Gradients of Recognition Molecules Shape Synaptic Specificity of Visuomotor Transformation

Mark Dombrovski[1], Yixin Zang[2#], Giovanni Frighetto[3#], Andrea Vaccari[4#], Hyojong Jang[5#], Parmis S. Mirshahidi[1#], Fangming Xie[1], Piero Sanfilippo[1], Bryce W. Hina[5], Aadil Rehan[1], Roni H. Hussein[1], Pegah S. Mirshahidi[1], Catherine Lee[1], Aileen Morris[1], Mark A. Frye[3], Catherine R. von Reyn[5], Yerbol Z. Kurmangaliyev[6], Gwyneth M. Card[2*] & S. Lawrence Zipursky[1*]

[1]Department of Biological Chemistry, David Geffen School of Medicine, University of California, Los Angeles, Los Angeles, CA, USA
[2]Department of Neuroscience, Howard Hughes Medical Institute, The Mortimer B. Zuckerman Mind Brain Behavior Institute, Columbia University, New York, NY, USA
[3]Department of Integrative Biology and Physiology, University of California, Los Angeles, Los Angeles, CA, USA
[4]Department of Computer Science, Middlebury College, Middlebury, VT, USA
[5]School of Biomedical Engineering, Science and Health Systems, Drexel University, Philadelphia, PA, USA
[6]Department of Biology, Brandeis University, Waltham, MA, USA

[#]Equal contributions

*Correspondence: S. Lawrence Zipursky (lzipursky@mednet.ucla.edu), Gwyneth M. Card (gc3017@columbia.edu)

Abstract

Converting sensory information into motor commands is fundamental to most of our actions[1,2]. In *Drosophila*, visuomotor transformations are mediated by Visual Projection Neurons (VPNs)[3,4]. These neurons encode object location and motion to drive directional behaviors through a synaptic gradient mechanism[5]. However, the molecular origins of such graded connectivity remain unknown. We addressed this question in a VPN cell type called LPLC2[6], which integrates looming motion and transforms it into an escape response through two separate dorsoventral synaptic gradients at its inputs and outputs. We identified two corresponding dorsoventral expression gradients of cell recognition molecules within the LPLC2 population that regulate this synaptic connectivity. Dpr13 determines synaptic outputs of LPLC2 axons by interacting with its binding partner, DIP-ε, expressed in the Giant Fiber – a neuron that mediates escape[7]. Similarly, Beat-VI regulates synaptic inputs onto LPLC2 dendrites by interacting with Side-II expressed in upstream motion-detecting neurons. Behavioral, physiological, and molecular experiments demonstrate that these coordinated molecular gradients regulate synaptic connectivity, enabling the accurate transformation of visual features into motor commands. As continuous variation in gene expression within a neuronal type is also observed in the mammalian brain[8], graded expression of cell recognition molecules may represent a common mechanism underlying synaptic specificity.

Main

Every day, we engage in a multitude of visually guided behaviors that rely on the conversion of an object's location in eye coordinates into directional body movements[9,10]. The brain regions and neural circuits responsible for these visuomotor transformations have been characterized in both vertebrates[11–13] and invertebrates[14,15]. These studies have revealed that learned visuomotor tasks[16–18] and innate visuomotor responses[19,20] rely on precise neuronal connectivity, which is established through genetically hardwired mechanisms, experience-dependent processes, or a combination of both.

In the fly brain, visuomotor transformation occurs between Visual Projection Neurons (VPNs) and Descending Neurons[21] (DNs, Fig. 1a). Although VPNs encompass a broad range of neuron types that connect the optic lobe to the central brain[22]; here we focus on well-characterized VPN sub-classes of columnar neurons[4], including LC (lobula columnar) and LPLC (lobula plate/lobula columnar). There are about 30 VPNs of these types, each comprising 20 to 200 neurons per brain hemisphere[3,4]. For simplicity, we will refer to these collectively as VPNs. The dendrites of individual neurons within a VPN type each span 20 to 40 degrees of visual space, while, as a population, they uniformly cover the optic lobe (Fig. 1a), creating a feature-detecting retinotopic map[23–25]. The axon terminals of each VPN type bundle together in the central brain, forming optic glomeruli, where some elaborate synapses onto the dendrites of DNs. For most of the VPN types, axonal retinotopy is lost[4,5], meaning the spatial organization of visual inputs onto VPN dendrites does not translate to their axonal arrangement in target glomeruli. We recently demonstrated that the transformation from visual input to motor output in VPN-DN circuits relies on a synaptic gradient mechanism, which in most cases functions independent of axonal retinotopy[5].

We define a synaptic gradient as a connectivity pattern in which the number of synapses connecting individual neurons within a presynaptic population (e.g., a VPN type) to postsynaptic targets (e.g., DNs) varies in a topographic fashion. For example, we found that within a population of looming-responsive VPNs, those with anterior receptive fields make more synapses onto DNs that drives a backward takeoff, while neurons with posterior receptive fields make more synapses onto DNs that drive a forward takeoff[5]. This anterior-posterior gradient of synapses enables the fly to detect looming threats and execute a rapid direction-specific escape response[5]. Overall, while synaptic gradients arise from retinotopically guided dendritic inputs, in most cases the resulting axonal synaptic connections represent visual space in a non-spatial, abstract manner. The molecular mechanism of such transformation remains unclear.

To uncover the molecular basis of synaptic gradients, we focused on a specific VPN type called lobula plate/lobula columnar 2 (LPLC2) neurons, a population of about 100 cells per hemibrain. Each LPLC2 neuron responds selectively to dark, radially-expanding motion stimuli centered on their receptive field, and, therefore act as local looming detectors[6,23]. The axons of LPLC2 neurons convey visual information to the Giant Fiber (GF), a DN that elicits a rapid escape takeoff in response to looming threats[7,29,30] (Fig. 1b). In our previous work, we showed that LPLC2 neurons elaborate a dorsoventral (DV) gradient of

synapses onto the GF through the analysis of electron microscopy (EM)-based connectomic reconstructions from two brain volumes[31,32–34]. LPLC2 neurons with dendrites sampling the dorsal part of the visual field form more synapses with the GF than their ventral counterparts (Fig. 1c-d).

Here, we investigated the molecular basis of the LPLC2-GF synaptic gradient by combining single cell RNA sequencing (scRNA-seq), spatial transcriptomics and genetics with morphological, behavioral, and physiological studies. We identified two cell recognition molecules expressed in a gradient across the LPLC2 population. One of them, *dpr13*, regulates connections of LPLC2 axons and the GF dendrites. The other, *beat-VI*, controls the formation of a synaptic gradient onto the dendrites of LPLC2 neurons. This shows that varying levels of cell recognition molecules within a defined neuronal type can specify different numbers of synapses both pre- and post-synaptically. Our findings represent a new mechanism of regulating synaptic specificity.

A Gradient of LPLC2-GF Synapses Shapes Escape Behavior

To assess the functionality of the DV synaptic gradient between LPLC2 and the GF, we quantified the escape response to looming stimuli from different parts of the visual field. Previous work showed that flies exhibit two modes of takeoff – a short mode using only leg extension, and a long mode using coordinated wing depression and leg extension[35] – and that short-mode takeoffs result solely from activation of the GF[7]. We therefore predicted that if LPLC2 neurons with more dorsal receptive fields made more synapses with the GF than ventral LPLC2 neurons, then we should observe more short-mode takeoffs in response to higher, compared to lower, elevations of a looming stimulus. To test this hypothesis, we analyzed thousands of previously collected[36] high-speed videos of takeoffs elicited by looming stimuli at different elevations to determine whether takeoff responses were short- or long-mode. As predicted, we found that the percentage of short-mode takeoffs steadily increased as the elevation of the looming stimulus increased from -30° to 77° (Fig. 1e, Extended Data Fig. 1a-c), as would be expected from higher engagement of the GF in response to more dorsal looming.

The GF receives direct visual input from only one other VPN type (LC4[36]) in addition to LPLC2. LC4 neurons do not form a DV synaptic gradient with the GF[5], suggesting the increase in GF-driven short-mode takeoffs at high elevations results directly from the LPLC2-GF synaptic gradient. We tested this by quantifying looming responses in flies with synaptic transmission from LPLC2 neurons blocked (Extended Data Fig. 1f-h). Without LPLC2 input, the percentage of short-mode takeoffs no longer changed across elevation (Extended Data Fig. 1h) and short-mode takeoff percentage was greatly reduced at high (77°) elevations compared to intact control flies.

We next directly tested whether differential LPLC2-GF connectivity along the DV axis biases GF activation. We performed in vivo whole-cell patch-clamp recordings in the GF during looming stimuli (horizontal arrays of small, expanding discs) at three elevations. We observed larger GF membrane depolarization in response to dorsal looming stimuli compared to ventral ones (Fig. 1f, Extended Data Fig. 1d-e). Together these results provide direct evidence that the DV

gradient in LPLC2-GF synaptic connections generates a corresponding DV gradient in GF activation, which ultimately influences escape behavior.

LPLC2 forms synaptic gradients without axonal retinotopy[4,5,37]. This means that GF dendrites form differential connections with intermingled LPLC2 axons. (Fig. 1g). We hypothesized that this pattern could be achieved through differential molecular recognition: individual LPLC2 neurons sampling different regions of visual space could express different levels of the same cell recognition molecule, which, in turn, would specify the number of synapses they form onto GF dendrites.

scRNA-seq Uncovers Molecular Heterogeneity in VPNs

To investigate whether LPLC2 neurons exhibit molecular variation that correlates with the synaptic gradient, we examined the LPLC2 transcriptome at three developmental stages during and after synaptogenesis (48, 72, and 96 hours after puparium formation (hAPF); Fig. 1h). In addition to LPLC2, we a related cell type, LPLC1, which also forms synaptic gradients without axonal retinotopy, but does not synapse onto the GF[5], and LC4, one of the few VPN cell types with axons arranged in a retinotopic fashion[5]. Given that neuronal transcriptomes are very dynamic during development and can be affected by genetic background[38], we introduced internal controls at each time point to account for transcriptional heterogeneity driven by these factors.

Briefly, we employed a genetic multiplexing strategy to perform pooled single-cell profiling across multiple biological replicates[38–40] (including different genetic backgrounds and developmental stages, see Methods). Our final dataset included approximately 600 high-quality single-cell transcriptomes per cell type and time point (Fig. 1i, Extended Data Fig. 2a-b). We validated the identity of each VPN cell type (LPLC2, LPLC1, or LC4) based on the expression of known marker genes[38], such as transcription factors (Fig. 1j, Extended Data Fig. 2a-b). This resulted in per-cell-type coverage roughly 30 times higher than in the existing single-cell atlases of the *Drosophila* optic lobes[38,41].

To explore heterogeneity in gene expression across each VPN cell type, we performed Principal Component Analysis (PCA) separately for each cell type and time point (Fig. 1k-m, Extended Data Fig. 2c-e, 3a-b). In LPLC2 neurons at 48h APF, the first principal component (PC1) captured a group of genes that were expressed in a graded manner across individual neurons (Fig. 1k). For example, the most differentially expressed gene across LPLC2 was *dpr13*, encoding a cell recognition protein of the Immunoglobulin Superfamily (IgSF)[42]. It displayed the highest magnitude of within-cell-type variation of expression. There was, however, no clear boundary separating neurons with high versus low *dpr13* expression levels. Many of the most differentially expressed genes also encode cell recognition molecules: IgSF (e.g., *tei*, *beat-VI*), Leucine-rich-repeat (e.g., *trn*) and Cadherin (e.g., *Cad87A*) families[28,42](Fig, 1k).

To test whether the transcriptional heterogeneity within LPLC2 neurons reflects discrete subtypes within the population or a continuous gradient, we analyzed the data by forcing the neurons into artificial clusters and then randomly shuffling gene expression in two ways: across all cells or only within artificial clusters (Extended Data Fig. 3c-g). Shuffling across all cells disrupted the original

gradient, indicating that the observed variation arises from coordinated gene expression. By contrast, shuffling gene expression only within arbitrarily separated clusters of neurons along the continuum introduced artificial gaps, showing that the original data do not naturally separate into discrete subtypes. These results demonstrate that the transcriptomic heterogeneity within LPLC2 neurons forms a smooth continuous gradient.

The distribution of neurons along PC1 also did not correlate with developmental age, sex, genetic background, or mRNA coverage (Fig. 1l, Extended Data Fig. 2e, 3a-b), indicating that the observed within-cell-type molecular heterogeneity had a different origin. The graded expression of the top differentially expressed genes associated with PC1 at 48h APF (*dpr13*, *beat-VI*, and *tei* (encoding IgSF molecules), as well as *SiaT* (encoding Sialyltransferase)) persisted through development (Fig. 1m).

In LPLC1 neurons, PC1 also captured gradients of transcripts encoding IgSF recognition molecules (e.g., *DIP-kappa*, *CG33543*, *dpr3*, *sdk*) that persisted through development (Extended Data Fig. 2c-d). Similar to LPLC2, molecular gradients in LPLC1 could not be explained by differences in age, sex, genetic background, or mRNA coverage across individual neurons (Extended Data Fig. 2e, 3a-b). By contrast, PC1 in LC4 correlated with the technical quality of single-cell transcriptomes (number of transcripts captured per each neuron, Extended Data Fig. 2e, 3a-b) suggesting that the molecular heterogeneity in LC4 neurons is not biologically relevant.

In summary, we uncovered persistent expression gradients of recognition molecules within LPLC1 and LPLC2 neurons. The absence of such gradients in LC4 neurons suggests that molecular heterogeneity within cell types may be a feature exclusive to VPNs that elaborate synaptic gradients independent of axon topography.

Spatial Transcriptomics Validates Molecular Gradients

We sought to independently verify gene expression gradients in LPLC2 neurons. To do this, we used Single-Molecule Hairpin Chain Reaction Fluorescent in Situ Hybridization[43] (HCR-FISH), a spatial transcriptomics method that allows for the quantification of gene expression in individual cells. Combined with Expansion-Assisted Light Sheet Microscopy[44], this approach enabled us to visualize and count individual transcripts within neuronal cell bodies (Fig. 2a). We observed that cell bodies of adjacent LPLC2 neurons exhibited striking differences in the numbers of mRNA transcripts for *dpr13* and *SiaT*, the two most differentially expressed genes in the LPLC2 dataset (Fig. 2b-c). Similar patterns were observed for *beat-VI* and *dpr17*, two differentially expressed genes encoding IgSF recognition molecules (Extended Data Fig. 4a-d).

To broaden our analysis to other genes, we tested pairs of genes that exhibited correlated or anticorrelated expression patterns based on scRNA-seq data (Fig. 1k) to determine if these relationships were replicated using HCR-FISH. We quantified differential gene expression using Flyseg[45], an automated volumetric instance segmentation algorithm we previously developed (see Methods). The results of scRNA-seq and HCR-FISH were similar for genes

exhibiting antiparallel (e.g., *dpr13* and *SiaT*, Fig. 2d, top) and parallel expression patterns (e.g., *dpr13* and *beat-VI*, Fig. 2d, bottom). Most of these relationships remained consistent throughout development (Fig. 2e, Supplemental Table 2), supporting our findings from scRNA-seq data. One exception was *mbl* (*muscleblind*); although this gene exhibited graded expression in scRNA-seq (Fig. 1k), it showed low, uniform expression in HCR-FISH. The reason for this discrepancy is unclear. Thus, the presence of gene expression gradients within the LPLC2 population seen in scRNA-seq data was also seen for most differentially genes in HCR-FISH.

Molecular Gradients Align with Synaptic Gradients

The cell bodies of the LPLC2 neurons where we measured different levels of transcripts were arranged in a salt-and-pepper fashion (Fig. 2c). LPLC2 dendrites are, however, retinotopically arranged. We next investigated whether there was a correlation between the retinotopic position of LPLC2 dendrites and the expression level of genes. To do this, we used a genetic intersection method to selectively visualize neurons within a specific cell type that express a particular gene at a given time point (Fig. 2f-g). Genes encoding recognition molecules *dpr13*, *beat-VI*, and *Cad87A*, which displayed correlated expression profiles in the scRNA-seq data (Fig. 1k), were predominantly expressed by LPLC2 neurons with dendrites in the dorsal region of the lobula at 48h APF (Fig. 2h-i, Extended Data Fig. 5a-b). Conversely, the expression of *SiaT*, *dpr17*, *CG03419*, *Tsp42Ef*, and *stacl* was limited to the ventral region at the same developmental stage (Fig. 2h-i, Extended Data Fig. 5c-d). We validated this DV heterogeneity using HCR-FISH, confirming that sparsely labeled dorsal LPLC2 contained significantly more *dpr13* and *beat-VI* transcripts than their ventral counterparts (Extended Data Fig. 4e-f). Heterogeneous expression of genes encoding recognition molecules *DIP-kappa*, *dpr17* and *sdk* in LPLC1 neurons had similar retinotopic correlates (Extended Data Fig. 5e-f), suggesting that such retinotopically biased expression gradients are a general feature of many VPN cell types.

To see if these transcriptional gradients are maintained at the protein level, we used MIMIC-based protein traps[46] generating GFP-tagged versions of two “dorsal” recognition proteins, Dpr13 and Beat-VI. This facilitated visualization of protein expression under their endogenous regulatory elements. Despite GFP accumulation in cell bodies (likely resulting from impaired trafficking due to truncation of GFP-tagged proteins), we observed significant GFP signal differences between dorsal and ventral LPLC2 neurons for both Dpr13 and Beat-VI, indicating that the trend in the mRNA level trend is preserved at the level of protein translation (Extended Data Fig. 4i-l).

In summary, we found that the dendrites of individual neurons within a single VPN cell type, sampling different regions of visual space, are molecularly heterogeneous. Across a VPN population, the neurons express gradients of recognition molecules that match the orientation of synaptic gradients in these VPNs. These findings suggest that, despite spatial intermingling, the axons retain distinct molecular identities. We next sought to determine if these molecular and synaptic gradients are functionally significant.

The Dpr13::DIP-ε gradient forms a looming escape synaptic gradient

LPLC2 neurons express genes encoding IgSF recognition proteins in a DV gradient, with *dpr13* and *beat-VI* having higher expression levels in dorsal LPLC2 neurons and *dpr17* higher expression in ventral ones. We hypothesized that one or more of these molecular gradients could specify the gradient in synapse number between LPLC2 axons and GF dendrites (Extended Data Fig. 6a). If this were the case, the GF would need to express cell surface proteins that bind to one or more of these three recognition molecules. This would allow the differential molecular expression in LPLC2 neurons to be converted into differential cell adhesion between individual LPLC2 neurons and the GF. Dpr proteins bind to DIP proteins, a related but different IgSF subfamily[42,47]. There are multiple paralogs of each, and interactions between them have been characterized[48]. Similarly, Beat proteins bind to Sides, also IgSF members[42,49] (Fig. 3a). To test our hypothesis, we assessed expression levels of genes encoding binding partners of Dpr13, Beat-VI and Dpr17 (DIP-ε, Side-II and DIP-γ, respectively) in the GF using HCR-FISH. *DIP-ε*, encoding a binding partner of Dpr13, was the only gene showing strong expression in the GF during development (Fig. 3b-c).

To determine if DIP-ε played a role in forming connections between LPLC2 axons and the GF dendrites, we next looked at the interaction between LPLC2 axons and GF dendrites in DIP-ε-deficient flies during development. In animals with no DIP-ε (*DIP-ε^{null}* allele), we observed a ~10-fold decrease in axo-dendritic overlap volume between LPLC2 axons and the GF dendrites (Fig. 3d-e). Wild type levels of axo-dendritic overlap could be restored in these *DIP-ε^{null}* flies by overexpression of *DIP-ε* in just the GF (Fig. 3f, Extended Data Fig. 6d). Knockdown of *DIP-ε* specifically in the GF using two different RNAi lines also significantly reduced LPLC2-GF axo-dendritic overlap (Fig. 3f, Extended Data Fig. 6c). To assess whether the reduced axo-dendritic overlap was associated with a decrease in synapse number between LPLC2 and the GF, we visualized presynaptic sites (marked with T-bar-associated endogenously tagged Bruchpilot (Brp) protein) in sparsely labeled LPLC2 neurons using a modification of the Synaptic Tagging with Recombination (STaR)[50] technique (Extended Data Fig. 7a-b). RNAi knockdown of *DIP-ε* in the GF led to a significant reduction in the number of LPLC2 T-bars contacting the GF dendrites (Extended Data Fig. 7c-f) Thus, DIP-ε is required in the GF to establish synaptic connectivity with LPLC2 axons.

If DIP-ε is required to form functional LPLC2-GF synapses, then we would expect that DIP-ε-deficient flies would have decreased GF responses to looming stimuli and exhibit fewer GF-driven “short-mode” takeoffs than control flies. Furthermore, we anticipated that, if too few LPLC2-GF synapses formed to make a DV gradient, then the number of short-mode takeoffs would no longer increase with increasing elevation of the looming stimulus. To check these hypotheses, we first performed whole-cell patch-clamp recordings in the GF while presenting looming stimuli. As predicted, we observed a reduction in the peak magnitude of the GF response in *DIP-ε^{null}* animals and in those expressing DIP-ε RNAi in the GF compared to controls (Fig. 3h-i; Extended Data Fig. 8). We next tested DIP-ε-

deficient flies in the FlyPEZ behavior apparatus. Both *DIP-ε*^{null} animals and animals expressing *DIP-ε* RNAi in the GF displayed a dramatic reduction in short-mode takeoff percentage at all stimulus elevations and a reduced difference between 0° and 77° elevations compared to the controls (Fig. 3j-k, Extended Data Fig. 9a-b). Together with our anatomical findings, these functional data further support a role for DIP-ε in the GF in establishing graded synaptic connectivity with LPLC2.

We next sought to test the causal role of the Dpr13::DIP-ε-defined gradient on takeoff behavior by retaining strong LPLC2-GF connectivity but eliminating the connectivity gradient. To achieve this, we increased the level of *dpr13* uniformly across the LPLC2 population (heretofore referred to as "overexpression") in otherwise wild type animals (i.e., superimposed upon the endogenous *dpr13* gradient). This increased the fold change in *dpr13* mRNA levels in ventral LPLC2 neurons more than their dorsal counterparts (193% vs 39%, Extended Data Fig. 4g). Compared to controls, animals overexpressing *dpr13* in LPLC2 exhibited a higher percentage of short-mode takeoffs mediated by the GF (Fig. 3l, Extended Data Fig. 9c). This gain-of-function was most pronounced at lower (0°) elevations, decreased at 45°, and was absent at higher (77°) stimulus elevations, resulting in no significant change in short-mode escape frequency with elevation. Thus, when *dpr13* is uniformly overexpressed across LPLC2 neurons, we observe an elimination of the DV gradient of short-mode takeoffs seen in control animals (Fig. 3l). Overexpression of *dpr13* also led to a modest increase in LPLC2-GF axo-dendritic overlap (Fig. 3m, Extended Data Fig. 6e). These data support a causal relationship between the level of *dpr13* and the number and graded distribution of LPLC2 synapses onto the GF.

We next sought to examine the consequences of removing dpr13 on the LPLC2-GF interaction. There was no difference between the LPLC2-GF axo-dendritic overlap volume and the number of LPLC2 T-bars contacting the GF dendrites in Dpr13 null mutant (*dpr13*^{null} allele) animals and controls (Fig. 3m, Extended Data Fig. 7c-f). This may be the result of redundancy, as LPLC2 neurons also express genes encoding four other DIP-ε-interacting dprs (*dpr14*, *dpr18*, *dpr19*, and *dpr20*; Extended Data Fig. 6h-i), which may compensate for the loss of *dpr13*. To address this, we ectopically expressed *DIP-ε* in LPLC2 with the intent of promoting *cis*-interactions between DIP-ε and all five Dpr paralogs, thereby inhibiting their *trans*-interactions with DIP-ε in the GF (an effect observed for other DIP/Dpr pairs[51,52]). This genetic manipulation reduced LPLC2-GF axo-dendritic overlap (Fig. 3o, Extended Data Fig. 6k-l), mimicking the phenotype of DIP-ε removal from the GF

Of the Dpr paralogs that bind to DIP-ε, however, only Dpr13 is expressed in a graded fashion (Extended Data Fig. 6j). Although loss of Dpr13 did not influence the overlap between LPLC2 axons and GF dendrites, *dpr13*^{null} animals no longer maintained the DV gradient of short mode takeoffs (Fig. 3n, Extended Data Fig. 9d). Surprisingly, this mainly resulted from a significantly increased short-mode takeoff percentage at lower stimulus elevations. This phenotype is similar to that observed when the difference in RNA levels across the population is reduced by uniformly overexpressing dpr13 in all LPLC2 neurons (Fig. 3l). The reason for this is not known. One interesting possibility it is that it is not the absolute level of Dpr13

that determines synapse number but rather the relative expression levels between different LPLC2 neurons across the dorsoventral axis (see *Discussion*).

In summary, DIP-ε and Dpr13 act as a ligand-receptor pair to control synaptic connectivity between LPLC2 and the GF. Our data support a model in which a DV gradient of Dpr13::DIP-ε interactions, shaped by graded expression of *dpr13* across LPLC2 neurons, specifies the formation of the DV gradient of synaptic weights (Fig. 3p).

Beat-VI::Side-II gradient forms a motion detection synaptic gradient

We next investigated the functional role of other genes that displayed gradients of expression across LPLC2 neurons (Fig. 1k). Like *dpr13*, *beat-VI*, another IgSF recognition molecule[53], was also expressed in a DV gradient in LPLC2 (higher expression in dorsal and lower in ventral LPLC2 – Fig. 2i, Extended Data Fig. 10a). However, loss of either Beat-VI or its binding partner, Side-II, did not affect the overlap between LPLC2 axon terminals and GF dendrites (Extended Data Fig. 10b-c). As LPLC2 dendrites also receive graded synaptic inputs (see below), we assessed whether the *beat-VI* gradient might function in LPLC2 dendrites rather than in axons.

We previously showed that Beat-VI regulates synaptic specificity in the *Drosophila* motion detection circuit[54], a finding that has since been corroborated by a more recent study[55]; Beat-VI and its interacting partner Side-II[53] are required for matching motion-detecting T4d/T5d neurons with their postsynaptic partners in layer 4 of the lobula plate (LoP4)[54,55], which encodes downward motion. Because LPLC2 is a part of this circuit, receiving excitatory inputs from T4/T5 neurons in all four LoP layers[6] (Fig. 4a, top), we hypothesized that the Beat-VI gradient might similarly influence LPLC2 dendritic connectivity.

Each LPLC2 neuron has four dendritic branches in the lobula plate, one in each layer, extending in four cardinal directions, corresponding to motion sensitivity in each layer[6] (Fig. 4a, bottom). The response measured at the LPLC2 axon is a non-linear sum of the activity in each of these four branches. Individual LPLC2 neurons thus serve as "looming detectors". They respond most strongly to looming stimuli that originate at their receptive field center extending radially outward simultaneously generating motion in all four cardinal directions, thereby maximally exciting each of the four dendritic branches[6]. Using "FAFB-Flywire"[32,34] connectome reconstruction, we found that two of the four classes of T4/T5 neurons, T4c/T5c and T4d/T5d, form antiparallel DV synaptic gradients onto LPLC2 dendrites in Lop3 and Lop4, respectively (Fig. 4b).

These findings suggest that dorsal and ventral LPLC2 neurons within one animal may receive differential amounts of upward and downward motion information, potentially linked to the molecular gradient of Beat-VI. Supporting this idea, RNAi knockdown of *beat-VI* differentially affected LPLC2 dendrites depending on their retinotopic location. LoP4 branches were missing in dorsal LPLC2, while central LPLC2 exhibited a milder phenotype, and ventral LPLC2 were unaffected (Fig. 4c-d – single cell sparse visualization, Extended Data Fig. 10d-e – whole population labeling). This suggests that ventral LPLC2 neurons utilize a Beat-VI-independent mechanism to extend their dendritic branch and

connect to other presynaptic partners in LoP4. Removing Side-II from T4/T5 neurons produced a similar graded phenotype affecting dorsal, but not ventral LPLC2 neurons (Fig. 4e), In other words, the severity of loss-of-function morphological phenotype was proportional to the expression level of *beat-VI* across the LPLC2 population.

Overexpression of *beat-VI* in LPLC2 caused the opposite graded effect: abnormal density of LoP4 dendritic branching was seen in ventral, but not dorsal, LPLC2 neurons (population level, Extended Data Fig. 10f). On a single-cell level, we observed an increase in LoP4 dendritic branch size in ventral LPLC2 neurons (population level, Extended Data Fig. 10g-h). This phenotype corresponded to a relatively stronger increase in *beat-VI* mRNA levels across ventral LPLC2 neurons, compared to their dorsal counterparts (280% vs 81%, Extended Data Fig. 4h). These results support the idea that DV-graded variations in Beat-VI and Side-II interactions differentially regulate the connectivity between T4d/T5d axons and LPLC2 dendrites.

To determine whether loss of Beat-VI in LPLC2 had functional effects, we performed a directional tuning experiment combined with calcium imaging in individual LPLC2 neurons. We imaged from the unbranched neurite that connects an LPLC2 dendrites in the Lobula plate to their dendrites in the Lobula (see Methods, Fig. 4f-h, Extended Data Fig. 11a). Neurites in this location were previously shown to have weak responses to a small bar moving in each of four cardinal directions (i.e., stimuli exciting LPLC2 dendrite branches in a single LoP layer) and a much larger response to looming (i.e., stimuli exciting LPLC2 dendritic branches in all four LoP layers simultaneously)[6].

Wild type dorsal and ventral LPLC2 neurons exhibited different patterns of responses to directional stimuli (Fig. 4i-l, Extended Data Fig 11b-d, 11f). Ventral LPLC2 showed little to no response to downward motion, as would be expected if they received little input from downward sensing T4d/T5d neurons in LoP layer 4 (Fig. 4b, 4i-l, Extended Data Fig. 11b-c, 11f). As a result, responses to stimuli were biased toward upward motion. In contrast, dorsal LPLC2 neurons were more omnidirectionally sensitive, as expected if synaptic inputs from all four LoP layers was more evenly balanced (Fig 4i-l, Extended Data Fig 11b-c, 11f). Notably, after *beat-VI* knockdown, dorsal LPLC2 neuron responses became biased for upward motion, making them similar to wild-type ventral neurons, consistent with downward-selective T4d/T5d input being reduced (i.e., loss of LoP4 dendritic branch, Fig. 4c). *beat-VI* knockdown had little effect on ventral LPLC2 neurons, which remained biased for upward motion (Fig. 4j-l, Extended Data Fig. 11c, f). The functional consequences of *beat-VI* overexpression in LPLC2 were opposite to *beat-VI* loss-of-function. No significant changes were seen in the responses of dorsal LPLC2 neurons. By contrast, ventral neurons displayed increased responses to downward motion, becoming omnidirectionally sensitive, and, thus, undistinguishable from wild-type dorsal neurons (Fig. 4j-l, Extended Data Fig. 11d, f). Thus, both *beat-VI* knockdown and overexpression disrupted the normal directional tuning biases across LPLC2 neurons (Fig. 4l) without significantly affecting their response differences to looming stimuli (Fig. 4m, Extended Data Fig. 11e).

In summary, Beat-VI and Side-II act as a ligand-receptor pair to control synaptic connectivity between T4d/T5d and LPLC2 neurons. Our data support a model in which the DV gradient of Beat-VI::Side-II interactions contributes to the formation of the DV gradient of synaptic weights between T4d/T5d and LPLC2 neurons. This results in a decrease in the response to downward motion by LPLC2 neurons with ventral receptive fields (Fig. 4n).

Discussion

In this study, we identified the molecular origins of two parallel dorsoventral synaptic gradients in the axons and dendrites of LPLC2, a looming-detecting VPN cell type. These synaptic gradients translate retinotopic information from the fly's visual field into specific motor outputs. We demonstrate that a gradient of Beat-VI protein interacting through its binding partner Side-II regulates the graded synaptic inputs from T4d/T5d neurons onto LPLC2. This regulates differential integration of the downward motion component in the looming stimulus across different regions of the eye. Similarly, a gradient of Dpr13 working through its binding partner DIP-ε, shapes the graded synaptic outputs of LPLC2 onto the GF. This biases the escape towards faster takeoffs in response to looming stimuli from the dorsal visual field. These synaptic gradients, however, are distinct from each other. For the dendritic synaptic gradient, there is a retinotopic match between populations of input neurons (T4d/T5d) and the postsynaptic LPLC2 neurons (i.e., *many-to-many with retinotopy*). By contrast, multiple LPLC2 axons form different numbers of synapses onto the dendrites of a single cell (GF) (i.e., *many-to-one without retinotopy*). Irrespective of these differences, our findings indicate that different levels of recognition molecules establish differences in synapse numbers, and these differences, in turn, regulate behavior.

What is the relationship between the parallel gradients of *beat-VI* and *dpr13* expression and the number of synaptic inputs to and outputs from LPLC2? In *beat-VI* loss and gain-of-function experiments, the severity of functional consequences was directly proportional to *beat-VI* expression levels in individual LPLC2 neurons. The morphological phenotypes were also similar whether *beat-VI* was removed from LPLC2 or *side-II* from T4/T5 neurons, with the reduction in LoP4 dendritic branching corresponding to *beat-VI* expression levels. However, it remains unclear whether this phenotype arises from a failure to extend dendrites, or to stabilize them. We propose that Beat-VI and Side-II promote adhesion between T4d/T5d axons and LPLC2 dendrites, with the strength of this adhesion correlating with *beat-VI* expression levels. This protein interaction could influence synapse number either indirectly, by increasing the area of contact between T4d/T5d axons and LPLC2 dendrites, or directly, by controlling synapse formation, with decreased synapse numbers leading to reduced axo-dendritic contact.

Dpr13 and DIP-ε are essential for establishing synaptic connections between LPLC2 neurons and the GF. Loss of DIP-ε function reduced the overlap between LPLC2 axons and the GF dendrites, leading to significant defects in GF responses to looming stimuli, as demonstrated by both behavioral and electrophysiological assays. Analyzing the loss of Dpr13 function is complicated

by the presence of four additional Dpr paralogs in LPLC2, interacting with DIP-ε with similar binding affinities. By ectopically expressing *DIP-ε* in LPLC2, we inhibited all DIP-ε-interacting Dprs in LPLC2. This phenocopied the DIP-ε loss-of-function phenotype in the GF, providing additional support for the interactions between DIP-ε in the GF dendrites with its cognate binding Dprs in LPLC2 axons.

The role of multiple Dpr paralogs interacting with DIP-ε may be to ensure baseline synaptic connectivity in the crucial escape circuit, while the formation of the synaptic gradient depends specifically on Dpr13 levels. In support of this, both gain and loss of Dpr13 function eliminated the graded behavioral response to dorsal versus ventral looming stimuli. These observations support the idea that Dpr13::DIP-ε interactions exert precise control over the number of synapses formed between two neurons, resulting in the formation of an ethologically relevant synaptic gradient between LPLC2 and the GF. Future studies will explore the molecular mechanisms by which this occurs.

The Dpr13::DIP-ε gradient functions differently from Eph and Ephrin gradients in vertebrate retinotectal maps[56,57]. Both gradients relay visual-spatial information from the eye to the brain but use distinct strategies. Ephrins and Ephs form topographic maps by maintaining the positional information of neurons in the retina to arrangement of their axons in the midbrain[58] (i.e., retinotopy). By contrast, the Dpr13::DIP-ε gradient translates positional information from VPN dendrites into synapse numbers in the central brain independent of axon retinotopy.

As most VPNs form synaptic gradients[5], varying levels of adhesion molecules may be a common mechanism for synapse number regulation. Notably, altering levels of SynCAM1, another IgSF adhesion molecule, also affects synapse numbers in the mammalian hippocampus[59]. Together, these data suggest that not only do the cell recognition molecules determine synaptic specificity by qualitatively matching synaptic partners[26–28], but that their expression levels may also influence the number of synapses formed between matched neurons with functional and behavioral consequences. This variation holds enormous potential for fine-tuning ethologically relevant behavioral responses driven by complex neural circuits.

Our work has uncovered graded molecular heterogeneity within single VPN cell types. This feature is distinct from discrete[38,41] or stochastic[60,61] variations in gene expression within neuronal types previously described in *Drosophila*. We identified many graded genes in VPNs beyond cell recognition molecules, suggesting that molecular gradients may regulate other cellular and circuit functions. These findings are particularly interesting as cell types in the mammalian cortex also exhibit spatially patterned continuous transcriptomic variation[8,62–65]. These data raise an interesting possibility that within-cell-type molecular variation could be a common mechanism for generating neuronal diversity which, in turn, contributes to synaptic specificity.

In conclusion, we describe a molecular strategy regulating neural circuit assembly. This was enabled through detailed EM-connectomics of the fly brain[22,31–34], rapid advances in single-cell sequencing technologies, genetics, physiology and behavior. We anticipate that merging these approaches to study

598 other circuits in fly and the mammalian brain[66,67] will uncover new molecular
599 mechanisms underlying wiring specificity.
600
601
602 ## References

603 1. Shin, S., Crapse, T. B., Angeles, L., Mayo, J. P. & Sommer, M. A.
604 Visuomotor Integration. *Encycl. Neurosci.* (2009).
605 2. Andersen, R. A., Snyder, L. H., Li, C. S. & Stricanne, B. Coordinate
606 transformations in the representation of spatial information. *Curr. Opin.*
607 *Neurobiol.* **3**, 171–176 (1993).
608 3. Otsuna, H. & Ito, K. Systematic analysis of the visual projection neurons of
609 Drosophila melanogaster. I. Lobula-specific pathways. *J. Comp. Neurol.*
610 **497**, 928–958 (2006).
611 4. Wu, M. *et al.* Visual projection neurons in the Drosophila lobula link feature
612 detection to distinct behavioral programs. *Elife* **5**, 1–43 (2016).
613 5. Dombrovski, M. *et al.* Synaptic gradients transform object location to
614 action. *Nature* **613**, 534–542 (2023).
615 6. Klapoetke, N. C. *et al.* Ultra-selective looming detection from radial motion
616 opponency. *Nature* **551**, 237–241 (2017).
617 7. Von Reyn, C. R. *et al.* A spike-timing mechanism for action selection. *Nat.*
618 *Neurosci.* **17**, 962–970 (2014).
619 8. Cembrowski, M. S. & Menon, V. Continuous Variation within Cell Types of
620 the Nervous System. *Trends Neurosci.* **41**, 337–348 (2018).
621 9. Ghahramani, Z., Wolpert, D. M. & Jordan, M. I. Generalization to local
622 remappings of the visuomotor coordinate transformation. *J. Neurosci.* **16**,
623 7085–7096 (1996).
624 10. Fujiwara, Y., Lee, J., Ishikawa, T., Kakei, S. & Izawa, J. Diverse coordinate
625 frames on sensorimotor areas in visuomotor transformation. *Sci. Reports*
626 *2017 71* **7**, 1–9 (2017).
627 11. Buneo, C. A., Jarvis, M. R., Batista, A. P. & Andersen, R. A. Direct
628 visuomotor transformations for reaching. *Nature* **416**, 632–636 (2002).
629 12. Helmbrecht, T. O., dal Maschio, M., Donovan, J. C., Koutsouli, S. & Baier,
630 H. Topography of a Visuomotor Transformation. *Neuron* **100**, 1429-
631 1445.e4 (2018).
632 13. Kim, J. H., Ma, D. H., Jung, E., Choi, I. & Lee, S. H. Gated feedforward
633 inhibition in the frontal cortex releases goal-directed action. *Nat. Neurosci.*
634 *2021 2410* **24**, 1452–1464 (2021).
635 14. Huston, S. J. & Jayaraman, V. Studying sensorimotor integration in insects.
636 *Curr. Opin. Neurobiol.* **21**, 527–534 (2011).
637 15. Cruz, T. L. & Chiappe, M. E. Multilevel visuomotor control of locomotion in
638 Drosophila. *Curr. Opin. Neurobiol.* **82**, 102774 (2023).
639 16. Wang, T. S. L., Martinez, M., Festa, E. K., Heindel, W. C. & Song, J. H.
640 Age-related enhancement in visuomotor learning by a dual-task. *Sci.*
641 *Reports 2022 121* **12**, 1–12 (2022).
642 17. Dombrovski, M. *et al.* A Plastic Visual Pathway Regulates Cooperative
643 Behavior in Drosophila Larvae. *Curr. Biol.* (2019)

644 doi:10.1016/j.cub.2019.04.060.
645 18. Zada, D. *et al.* Development of neural circuits for social motion perception
646 in schooling fish. *Curr. Biol.* **0**, (2024).
647 19. Wei, P. *et al.* Processing of visually evoked innate fear by a non-canonical
648 thalamic pathway. *Nat. Commun. 2015 61* **6**, 1–13 (2015).
649 20. Zhao, P. *et al.* The visuomotor transformations underlying defensive
650 behaviors and hunting. *bioRxiv* 2024.05.07.592863 (2024)
651 doi:10.1101/2024.05.07.592863.
652 21. Cande, J. *et al.* Optogenetic dissection of descending behavioral control in
653 Drosophila. *Elife* **7**, (2018).
654 22. Nern, A. *et al.* Connectome-driven neural inventory of a complete visual
655 system. *bioRxiv* 2024.04.16.589741 (2024)
656 doi:10.1101/2024.04.16.589741.
657 23. Klapoetke, N. C. *et al.* A functionally ordered visual feature map in the
658 Drosophila brain. *Neuron* **110**, 1700-1711.e6 (2022).
659 24. Aptekar, J. W., Keleş, M. F., Lu, P. M., Zolotova, N. M. & Frye, M. A.
660 Neurons forming optic glomeruli compute figure–ground discriminations in
661 Drosophila. *J. Neurosci.* **35**, 7587–7599 (2015).
662 25. Keleş, M. F. & Frye, M. A. Object-Detecting Neurons in Drosophila. *Curr.*
663 *Biol.* **27**, 680–687 (2017).
664 26. Margeta, M. A. & Shen, K. Molecular mechanisms of synaptic specificity.
665 *Mol. Cell. Neurosci.* **43**, 261–267 (2010).
666 27. Südhof, T. C. Towards an Understanding of Synapse Formation. *Neuron*
667 **100**, 276 (2018).
668 28. Sanes, J. R. & Zipursky, S. L. Synaptic Specificity, Recognition Molecules,
669 and Assembly of Neural Circuits. *Cell* **181**, 536–556 (2020).
670 29. Bacon, J. P. & Strausfeld, N. J. The dipteran 'Giant fibre' pathway: neurons
671 and signals. *J. Comp. Physiol. A* **158**, 529–548 (1986).
672 30. Jang, H., Goodman, D. P., Ausborn, J. & von Reyn, C. R. Azimuthal
673 invariance to looming stimuli in the Drosophila giant fiber escape circuit. *J.*
674 *Exp. Biol.* **226**, (2023).
675 31. Scheffer, L. K. *et al.* A connectome and analysis of the adult drosophila
676 central brain. *Elife* **9**, 1–74 (2020).
677 32. Zheng, Z. *et al.* A Complete Electron Microscopy Volume of the Brain of
678 Adult Drosophila melanogaster. *Cell* **174**, 730-743.e22 (2018).
679 33. Dorkenwald, S. *et al.* Neuronal wiring diagram of an adult brain. *Nature*
680 **634**, 124–138 (2024).
681 34. Schlegel, P. *et al.* Whole-brain annotation and multi-connectome cell typing
682 of Drosophila. *Nature* **634**, 139–152 (2024).
683 35. Card, G. & Dickinson, M. H. Visually Mediated Motor Planning in the
684 Escape Response of Drosophila. *Curr. Biol.* **18**, 1300–1307 (2008).
685 36. Williamson, R., Peek, M. Y., Breads, P., Coop, B. & Card, G. M. Tools for
686 Rapid High-Resolution Behavioral Phenotyping of Automatically Isolated
687 Drosophila. *Cell Rep.* **25**, (2018).
688 37. Moreno-Sanchez, A. *et al.* Morphology and synapse topography optimize
689 linear encoding of synapse numbers in Drosophila looming responsive

descending neurons. *Elife* **13**, (2024).
38. Kurmangaliyev, Y. Z., Yoo, J., Valdes-Aleman, J., Sanfilippo, P. & Zipursky, S. L. Transcriptional Programs of Circuit Assembly in the Drosophila Visual System. *Neuron* **108**, 1045-1057.e6 (2020).
39. Kang, H. M. *et al.* Multiplexed droplet single-cell RNA-sequencing using natural genetic variation. *Nat. Biotechnol. 2017 361* **36**, 89–94 (2017).
40. MacKay, T. F. C. *et al.* The Drosophila melanogaster Genetic Reference Panel. *Nature* **482**, 173–178 (2012).
41. Özel, M. N. *et al.* Neuronal diversity and convergence in a visual system developmental atlas. *Nature* **589**, 88–95 (2021).
42. Özkan, E. *et al.* An extracellular interactome of immunoglobulin and LRR proteins reveals receptor-ligand networks. *Cell* **154**, 228 (2013).
43. Choi, H. M. T. *et al.* Third-generation in situ hybridization chain reaction: multiplexed, quantitative, sensitive, versatile, robust. *Development* **145**, (2018).
44. Lillvis, J. L. *et al.* Rapid reconstruction of neural circuits using tissue expansion and light sheet microscopy. *Elife* **11**, 1–36 (2022).
45. Vaccari, A. & Dombrovski, M. FlySeg: An Automated Volumetric Instance Segmentation Algorithm for Dense Cell Populations in Drosophila Melanogaster Nervous System. *Conf. Rec. - Asilomar Conf. Signals, Syst. Comput.* 1474–1478 (2023) doi:10.1109/IEEECONF59524.2023.10476819.
46. Nagarkar-Jaiswal, S. *et al.* A library of MiMICs allows tagging of genes and reversible, spatial and temporal knockdown of proteins in Drosophila. *Elife* **4**, (2015).
47. Cosmanescu, F. *et al.* Neuron-Subtype-Specific Expression, Interaction Affinities, and Specificity Determinants of DIP/Dpr Cell Recognition Proteins. *Neuron* **100**, 1385-1400.e6 (2018).
48. Sergeeva, A. P. *et al.* DIP/Dpr interactions and the evolutionary design of specificity in protein families. *Nat. Commun. 2020 111* **11**, 1–14 (2020).
49. Li, H. *et al.* Deconstruction of the beaten path-sidestep interaction network provides insights into neuromuscular system development. *Elife* **6**, 1–24 (2017).
50. Chen, Y. *et al.* Cell-type-specific labeling of synapses in vivo through synaptic tagging with recombination. *Neuron* **81**, 280–293 (2014).
51. Menon, K. P., Kulkarni, V., Shin-Ya, T., Anaya, M. & Zinn, K. Interactions between dpr11 and dip-y control election of amacrine neurons in drosophila color ision circuits. *Elife* **8**, 1–32 (2019).
52. Morano, N. C. *et al.* Cis inhibition of co-expressed DIPs and Dprs shapes neural development. *bioRxiv* 2024.03.04.583391 (2024) doi:10.1101/2024.03.04.583391.
53. Li, H. *et al.* Deconstruction of the beaten path-sidestep interaction network provides insights into neuromuscular system development. *Elife* **6**, (2017).
54. Yoo, J. *et al.* Brain wiring determinants uncovered by integrating connectomes and transcriptomes. *Curr. Biol.* **33**, 3998-4005.e6 (2023).
55. Carrier, Y. *et al.* Biased cell adhesion organizes the Drosophila visual

motion integration circuit. *Dev. Cell* (2024) doi:10.1016/J.DEVCEL.2024.10.019.

56. Brown, A. *et al.* Topographic mapping from the retina to the midbrain is controlled by relative but not absolute levels of EphA receptor signaling. *Cell* **102**, 77–88 (2000).
57. Triplett, J. W. & Feldheim, D. A. Eph and ephrin signaling in the formation of topographic maps. *Semin. Cell Dev. Biol.* **23**, 7 (2012).
58. Kita, E. M., Scott, E. K. & Goodhill, G. J. Topographic wiring of the retinotectal connection in zebrafish. *Dev. Neurobiol.* **75**, 542–556 (2015).
59. Robbins, E. M. *et al.* SynCAM 1 Adhesion Dynamically Regulates Synapse Number and Impacts Plasticity and Learning. *Neuron* **68**, 894–906 (2010).
60. Wernet, M. F. *et al.* Stochastic spineless expression creates the retinal mosaic for colour vision. *Nature* **440**, 174–180 (2006).
61. Miura, S. K., Martins, A., Zhang, K. X., Graveley, B. R. & Zipursky, S. L. Probabilistic splicing of Dscam1 establishes identity at the level of single neurons. *Cell* **155**, 1166 (2013).
62. Cembrowski, M. S. & Spruston, N. Heterogeneity within classical cell types is the rule: lessons from hippocampal pyramidal neurons. *Nat. Rev. Neurosci. 2019 204* **20**, 193–204 (2019).
63. Cheng, S. *et al.* Vision-dependent specification of cell types and function in the developing cortex. *Cell* **185**, 311-327.e24 (2022).
64. Yao, Z. *et al.* A taxonomy of transcriptomic cell types across the isocortex and hippocampal formation. *Cell* **184**, 3222-3241.e26 (2021).
65. Zeng, H. What is a cell type and how to define it? *Cell* **185**, 2739–2755 (2022).
66. Sievers, M. *et al.* Connectomic reconstruction of a cortical column. *bioRxiv* 2024.03.22.586254 (2024) doi:10.1101/2024.03.22.586254.
67. Yao, Z. *et al.* A high-resolution transcriptomic and spatial atlas of cell types in the whole mouse brain. *Nature* **624**, 317–332 (2023).
68. Gramates, L. S. *et al.* FlyBase: a guided tour of highlighted features. *Genetics* **220**, (2022).
69. Kang, H. M. *et al.* Multiplexed droplet single-cell RNA-sequencing using natural genetic variation. *Nat. Biotechnol. 2017 361* **36**, 89–94 (2017).
70. Li, H. A statistical framework for SNP calling, mutation discovery, association mapping and population genetical parameter estimation from sequencing data. *Bioinformatics* **27**, 2987–2993 (2011).
71. Hao, Y. *et al.* Dictionary learning for integrative, multimodal and scalable single-cell analysis. *Nat. Biotechnol.* **42**, 293–304 (2024).
72. Gabbiani, F., Krapp, H. G. & Laurent, G. Computation of Object Approach by a Wide-Field, Motion-Sensitive Neuron. *J. Neurosci.* **19**, 1122–1141 (1999).
73. Frighetto, G. & Frye, M. A. Columnar neurons support saccadic bar tracking in Drosophila. *Elife* **12**, (2023).
74. Reiser, M. B. & Dickinson, M. H. A modular display system for insect behavioral neuroscience. *J. Neurosci. Methods* **167**, 127–139 (2008).
75. Zhao, A. *et al.* Eye structure shapes neuron function in Drosophila motion

vision. *bioRxiv* 2022.12.14.520178 (2022) doi:10.1101/2022.12.14.520178.
76. DeBruine, L. M. & Barr, D. J. Understanding Mixed-Effects Models Through Data Simulation. *Adv. Methods Pract. Psychol. Sci.* **4**, (2021).
77. Saravanan, V., Berman, G. J. & Sober, S. J. Application of the hierarchical bootstrap to multi-level data in neuroscience. *Neurons, Behav. data Anal. theory* **3**, (2020).
78. Xu, S. *et al.* Interactions between the Ig-Superfamily Proteins DIP-α and Dpr6/10 Regulate Assembly of Neural Circuits. *Neuron* **100**, 1369-1384.e6 (2018).
79. Xu, H. *et al.* Sequence determinants of improved CRISPR sgRNA design. *Genome Res.* **25**, 1147–1157 (2015).
80. Ren, X. *et al.* Optimized gene editing technology for Drosophila melanogaster using germ line-specific Cas9. *Proc. Natl. Acad. Sci. U. S. A.* **110**, 19012–19017 (2013).
81. Wassie, A. T., Zhao, Y. & Boyden, E. S. Expansion microscopy: principles and uses in biological research. *Nat. Methods* **16**, 33–41 (2019).
82. Wang, Y. *et al.* EASI-FISH for thick tissue defines lateral hypothalamus spatio-molecular organization. *Cell* **184**, 6361-6377.e24 (2021).
83. Lee, P. T. *et al.* A gene-specific T2A-GAL4 library for Drosophila. *Elife* **7**, (2018).
84. Nern, A., Pfeiffer, B. D. & Rubin, G. M. Optimized tools for multicolor stochastic labeling reveal diverse stereotyped cell arrangements in the fly visual system. *Proc. Natl. Acad. Sci. U. S. A.* **112**, E2967–E2976 (2015).
85. Matsliah, A. *et al.* Neuronal parts list and wiring diagram for a visual system. *Nature* **634**, 166–180 (2024).

Materials and Methods

Experimental model details

Flies were reared under standard conditions at 25 °C and 50% humidity with a 12-h light/12-h dark cycle on a standard cornmeal fly food. Males and females 1-3 days after eclosion were used for all experiments except where specified. Supplementary Table 1 provides detailed descriptions of fly genotypes used in each experiment and origins of transgenic stocks. For developmental experiments, white pre-pupae (0h APF) were collected and incubated at 25 °C for the indicated number of hours.

scRNA-seq experiment

Virgin females carrying LPLC2, LPLC1 or LC4 split-GAL4 driver lines were crossed to males expressing a nuclear GFP reporter (UAS-His2A-GFP) and carrying unique 3rd chromosomes from the isogenic wild-type strains with known genotypes (DGRP, *Drosophila* Reference Genetic Panel[40]). Each experimental condition (cell type and time point) was crossed to 6 unique DGRP strains (see

Supplemental Table 1 and Source Data for details; LC4 driver was crossed into 4 DGRP strains for 72 and 96h APF time points). Each of these crosses was considered an independent biological replicate. F1 generation animals (males and females) were collected at 0h APF and incubated for either 48h, 72h or 96 hours at 25°C. To introduce a control for developmental age, we split 6 DGRPs (for each cell type and time point) into equal "early" and "late" groups (Fig. 1g, see Source data for a detailed breakdown). Animals from "early" DGRPs were continuously staged and collected within the 2h time window, after which we continuously staged and collected animals from "late" DGRPs within the next 2h time window. This ensured that by the time brains were dissected (after 48, 72 or 96 hours), animals from the "early" group were on average 2h older than their "late" counterparts. Brains were dissected in ice-cold Schneider's *Drosophila* Medium (GIBCO #21720-024), collected in three Eppendorf tubes (each time point was processed as a separate sample) and kept on ice. Brains were incubated in mix of papain (Worthington #LK003178, 1000 units/ml) and Liberase™ (Sigma-Aldrich #5401119001, 0.18 Wu/ml) at 25°C for 30 min shaking at 1000rpm, washed twice with 2% Bovine Serum Albumin (BSA, Sigma #B6917) in Schneider's Medium, followed by two washes in 1% BSA in PBS. Finally, brains were transferred to 0.04% BSA in PBS and dissociated mechanically by pipetting. The cell suspension was filtered through a 20 µm cell-strainer (Corning #352235) and sorted by FACS (BD FACS Aria II) to purify GFP+ cells. Single-cell suspensions were used to generate scRNA-seq libraries using the 10X Genomics Chromium Next GEM Single Cell 3'-kit (v3.1) following the manufacturer's protocol. Each sample (corresponding to a single time point) was loaded to a single lane of 10X Chromium. Three scRNA-seq libraries were sequenced using one lane of NovaSeq 6000 SP platform (28bp + 91 bp). The library preparation and sequencing were performed by the Technology Center for Genomics and Bioinformatics at UCLA.

scRNA-seq data processing and analysis

Raw scRNA-Seq reads were processed using Cell Ranger (10X Genomics, version: 7.1.0). The reference genome and gene annotations were downloaded from FlyBase[68] (release 6.29). Each time point was processed separately. Six biological replicates were tagged with a unique wild-type chromosome, and demultiplexed based on a unique wild-type chromosome using demuxlet[69] (version 2, https://github.com/statgen/popscle). Demultiplexing was performed using single-nucleotide polymorphisms (SNPs) from 7 DGRP strains used in experiments (see supplemental table 1 for the full list of genotypes and Source Data for the list of DGRP strains used for each genotype and time point) and 3 additional DGRP strains as negative controls (line_129, line_427, line 712). SNPs were filtered using the following criteria: (1) only bi-allelic SNPs on the 3rd chromosome without missing data (called in all 10 strains); (2) non-reference allele only in 1 of 10 strains. We quantified allelic counts for filtered SNPs using samtools mpileup[70] (version 1.10). SNPs with a minimum total coverage of 10 in all three samples (time points) and a maximum non-reference allele frequency of 0.25 were kept for downstream analysis (34,655 SNPs). Only a few cells (0.1-0.2%) were

erroneously assigned to negative controls; 5–15% of cells were classified as "doublets" and "ambiguous" (mostly cells with low transcript coverage). We removed cells with less than 10,000 or more than 50,000 transcripts per cell (and more than 10% of mitochondrial transcripts). The final dataset included 2,595 cells for 48h APF, 2,369 cells for 72h APF, and 1,039 cells for 96h APF.

The scRNA-seq analysis was performed using Seurat[71] package (5.0.1). The analysis was performed separately for each time point using the standard Seurat workflow: raw transcript counts were normalized, 1000 highly variable genes were scaled and used for PCA, first 5 PCs were used for clustering (resolution: 0.05) and to calculate t-SNE projections. We use t-SNE projection only for the summary visualization of the dataset. Clusters were annotated based on known marker genes[38] (Fig. 1i-j and Extended Data Fig. 2a-b). Most of the cells corresponded to LPLC2, LPLC1, and LC4 neurons. To explore further heterogeneity within VPN type, we subsetted each cell type at each time point, identified 500 highly variable genes, and repeated PCA. We plotted known biological and technical covariates along each analyzed PC (Fig. 1l and Extended Data Fig. 2-3), including developmental age, DGRP genotype, sex, and coverage (i.e., transcripts per cell). PC1s in LPLC2 and LPLC1 did not correlate with any of these covariates and were driven by similar sets of genes (Fig. 1l, m and Extended Data Fig. 2c-d). Further *in vivo* validations using orthogonal approaches confirmed that these PCs captured true molecular heterogeneity within each of these cell types (Fig. 2).

Behavioral experiments

High-throughput takeoff assay

High-throughput takeoff assay was performed with the FlyPEZ system, which allows for the near-automated collection of fly behaviors in response to visual stimulation in large sample sizes. FlyPEZ experiments were performed as previously described[36]. Briefly, untrained flies (3-5 days old, both males and females) were individually dispensed onto a 5 mm by 5 mm glass recording platform via an automated "FlyGate" module[36], which controls the opening and closing of the gate using a laser light sheet and linear photodetector. Once the fly reaches the platform, four mirrors allow simultaneous recording of two views of the fly (a bottom view and a side view) onto a single camera lens, which enables real-time detection of the center of mass and heading of the fly via the "FlyDetect" algorithm. The heading direction is then used to generate looming stimulation in fly coordinates, and the behavioral response of the fly is recorded by a high-speed camera at 6,000 frames per second under infrared illumination. A single stimulus was presented per fly. All behavioral experiments were performed 4 hours before incubator lights were switched off, which coincides with the flies' activity peak in the afternoon light cycle.

Visual stimulation for behavioral assay

A 7-inch-diameter back-projection coated dome is placed centered over the glass platform to present visual stimulation. Specifically, dark looming disks that approach the fly from azimuth of 0° (front looms) or 90° (side looms), at elevations

of -30°, 0°, 23°, 45°, or 77° in fly coordinates were used. Looming stimuli were generated using the same equation as described for calcium imaging experiments (see below). All looming stimuli have l/v=40ms. Experiments in Fig. 1e and Ext. Fig. 1a-c show trials that were performed in the past (from 2014 to 2024) using control flies shown looming disks with a starting size ranging from 1°-30° expanding to either 45°, 90° or 180°. Experiments in Fig. 3 include trials with looming disks expanding from 10° to 180° only.

Behavioral data analysis

To quantify the duration of the takeoff sequence, videos were manually annotated to identify the start of the sequence (the first frame of wing-rising) and the end of the sequence (the last frame that shows T2 legs in contact with the platform). Takeoff sequence durations between 0ms to 7ms were considered "short-mode takeoffs," and takeoff sequence durations longer than 7ms were considered "long-mode takeoffs," as described previously[7]. The total takeoff percentage is calculated by the number of takeoffs divided by the total number of trials. Short-mode takeoff percentage is calculated by the number of short-mode takeoffs divided by the total number of takeoffs. For experiments in Fig. 1e and Ext. Fig 1a-c, takeoff sequence duration longer than 50ms was eliminated as outliers. All takeoff sequence durations were less than 50ms for experiments in Fig. 3.

Statistical analysis

Statistical comparison of the percentages of short-mode takeoffs was performed with the Chi-squared test, with post-hoc Bonferroni correction for multiple comparisons. Statistical comparison of takeoff sequence distributions between two samples was performed with the Mann-Whitney U test. Statistical comparison of takeoff sequence distributions between more than two samples was performed with the Kruskal-Wallis test, with post-hoc Dunn correction for multiple comparisons. Analysis and plotting were conducted with custom scripts in MATLAB 2022b, and Scipy and Seaborn in Python 3.

Electrophysiological experiments

Electrophysiological recordings

In vivo whole-cell, current-clamp electrophysiology was performed on behaving, tethered flies as previously described[30]. Flies were anesthetized at 4°C and their head and thorax were attached to polyether ether ketone plates with UV glue (Loctite 3972). The T1 legs were severed at the femur to prevent cleaning of the head and obstruction of the eyes. The proboscis was secured in its retracted position to minimize brain movement during the recording. The antennae were also fixed with UV glue to restrict stimulation of antennal afferents to the GF. To access the GF for recordings, the cuticle and trachea on the posterior side of the head above the GF soma were removed and the brain was perfused with standard extracellular saline (NaCl 103 mmol, KCl 3 mmol, TES 5 mmol, trehalose-$2H_2O$ 8 mmol, glucose 10 mmol, $NaHCO_3$ 26 mmol, NaH_2PO_4 1 mmol, $CaCl_2 \cdot 2H_2O$ 1.5 mmol, and $MgCl_2 \cdot 6H_2O$ 4 mmol; Gouwens and Wilson 2009). Osmolarity was

adjusted to 270–275 mOsm and bubbled with 95% O2/5% CO2 to maintain a pH of 7.3. All experiments were conducted at room temperature (20–22°C). A brief, localized application of collagenase (0.5% in extracellular saline) with a glass electrode was used to disrupt the brain sheath and access the soma for recording. GFP-labeled soma was then targeted by patch-clamp electrodes (4–6 MΩ) containing intracellular saline (potassium aspartate 140 mmol, KCl 1 mmol, Hepes 10 mmol, EGTA 1 mmol, Na_3GTP 0.5 mmol, MgATP 4 mmol, Alexafluor-568 5 µmol, 265 mOsm, pH 7.3). In vivo whole-cell recordings were performed in current-clamp mode using a MultiClamp 700B amplifier, and digitized (NI-DAQ, National Instruments) at 20 kHz. Data were acquired using either the open-source software Wavesurfer (https://wavesurfer.janelia.org/) running in MATLAB (MathWorks), or Clampex. Traces were not corrected for a 13-mV liquid junction potential (Gouwens and Wilson, 2009). Recordings were considered acceptable when the initial seal resistance was >2 GΩ before rupture, the resting membrane potential was less than −50 mV, and the input resistance was >50 MΩ, as the typical input resistance of the GF has been reported to be in the range of 50 to 100 MΩ.

Visual stimulation for electrophysiology and data analysis

Visual stimuli were back-projected onto a 4.5-inch diameter mylar cylindrical screen covering 180 degrees in azimuth via two DLP projectors (Texas Instruments Lightcrafter 4500) as previously described[33]. The projected images were displayed in 6-bit grayscale at 240Hz, above the flicker fusion frequency of Drosophila (100Hz; Niven et al., 2003). All stimulus frames were generated in MATLAB and presented using Psychtoolbox (http://psychtoolbox.org/). Looming stimuli were generated with the background set to white and the expanding disk (looming stimulus) set to black on the projector (5500 lx-white and 15 lx-black, measured at the position of the fly). The angular size (θ) of the stimulus subtended by the approaching object was calculated in time (t) by the following equation[72]:

$$\theta(t) = 2tan^{-1}\left(\frac{r}{vt}\right),$$

where t<0 before collision and t=0 at collision for an approaching object with a radius (r) and constant velocity (v). As previously described[72], r/v (ms) is the radius to approach speed ratio. The smaller the r/v, the more abrupt the stimulus expansion. The visual stimulus set consisted of four looming stimuli (r/v=10, 20, 40, 80 ms) starting at 10 degrees and expanding to 63 degrees in angular size and held for 1 second, displayed at −45 degrees in azimuth, 0 degrees in elevation. Each visual stimulus was presented once per trial, in a randomized order. Interstimulus intervals were set to 30 seconds to allow enough time for the GF membrane potential to return to baseline and avoid habituation. The responses to the same stimulus from two successive trials were then averaged for each fly.
Electrophysiology data distributions were evaluated using a Kolmogorov-Smirnov test. If the data were found not to follow a normal distribution, the appropriate non-parametric test was selected. Statistical comparison of GF's looming responses between two groups was performed with the Mann-Whitney U test.

For electrophysiology experiments in Fig. 1, visual stimuli were back-projected at 360 Hz onto a 4-inch diameterdome at 768 × 768 resolution as previously described (Dombrovski et al., 2023). Looming visual stimuli were generated using Psychtoolbox as mentioned previously. To maximize GF responses, a column of three black looming disks was displayed on a white background on the experimentally accessible visual field of the fly from elevation of -25° to 25°. The looming disks expand from 0° to 30° at a constant velocity of 500°/s. Looming stimuli from different elevations were shown in randomized order for five times per animal, with a 15s inter-stimulus interval. The baseline region of each trial corresponded to the 2s time window before the onset of the looming stimulus, and the response region was the 150ms period after the onset of the stimulus. To estimate the magnitude of depolarization in response to looming stimuli, membrane potentials were averaged across individual trials, and the peak response (mV) and area (ms × mV) relative to the baseline were calculated in the 150ms response region using custom Matlab scripts. Statistical comparison of GF's looming responses across elevations was performed with repeated-measures one-way ANOVA test, with post-hoc Sidak correction for multiple comparisons.

Two-photon calcium imaging experiments

Imaging setup

Calcium imaging was performed with a VIVO Multiphoton Open (Intelligent Imaging Innovation, Inc.) system based on a Movable Objective Microscope (MOM, Sutter Instruments). The excitation of the sample was delivered by a Ti:Sapphire laser (Chameleon Vision I, Coherent) tuned to 920 nm with power ranging from 15 to 30 mW (depending on imaging depth). A dual axis mirror galvanometer was used for x-y laser scanning (RGG scanbox, Sutter Instrument). We imaged with a 20x water-immersion objective (W Plan-Apochromat 20x/1.0 DIC, Zeiss) and a band-pass filter (Semrock 525/40 nm) was placed in front of the photomultiplier tube (H11706P-40, Hamamatsu) to reduce the blue light from the visual display. Microscope and data acquisition were controlled by Slidebook 2024 (Intelligent Imaging Innovation, Inc.). Single plane images were sampled at 9 Hz with a spatial resolution of approximately 180 x 180 pixels (95.7 x 95.7 µm, pixel size ≅ 0.53 µm, dwell time ≅ 2 µs). Images and external visual stimuli were synchronized *a posteriori* using frame capture markers (TTL pulses from Slidebook 2024) and stimulus events (analog outputs from the visual display) sampled with a data acquisition device (USB-6229, National Instruments) at 10 kHz.

Fly tethering and preparation for imaging

Flies were prepared and head-fixed to a custom objective stage fly holder as previously described[73]. The cuticle above the right optic lobe was removed and the brain bathed in isotonic saline. The holder with the tethered fly was placed under the objective at the center of the visual display in the horizontal plane. GCaMP7f responses of dendritic branches from individual LPLC2 neurons were recorded from a posterior view. The fly head was pitched forward pointing down at the visual display so that the fly eye's equator held a pitch angle of approximately 60° relative

to the imaging plane. For each fly, we identified the most dorsocaudal dendritic arbors in the lobula plate and then moved the focal plane ~10 µm below them to start mapping the receptive field (RF) centers of dorsal LPLC2 neurons, or moved ~50 µm to probe ventral LPLC2 RFs, similarly to previous calcium imaging experiments in LPLC2[6]. Random steps (± 5 µm) between these two bracketed Z-planes were used to probe the RF centers of dorsoventrally intermediate LPLC2 neurons. Unstable recordings or recordings from preparations that did not respond during the RF scanning trials were not included in the data set.

Visual stimuli for imaging

A visual display composed of 48 8x8 dot matrix LED panels arranged in a semi-cylinder[74] was used for visual stimulation as previously described[73]. Four layers of filter (071, LEE Filters) were placed over the display to reduce its light intensity. To compensate for the angle of the eye's equator and optimize the extension of the surrounding visual context, the display was tilted forward at an angle of 30° from the horizontal plane. Visual presentation was confined to the right half of the visual field, ipsilateral to the recording site. Visual stimuli were generated and controlled using custom-written MATLAB (MathWorks) scripts that communicated to the display through the microcontroller serial port. Looming stimuli simulated an object approaching the fly at a constant velocity, equivalent to twice the inverse tangent of the ratio between object's half-size and object's approach speed (see description of electrophysiological experiments). The display background was set to 70% maximum intensity while foreground objects (looming or moving bars) were set to 0%. The set of visual stimuli was presented in random block design and repeated 2 times. Each visual stimulation lasted 4 s and was composed by 0.5 s of uniform background, and 0.5 s of visual motion followed by 3 s of static pattern. Each trial was followed by 3 s of rest in which flies faced the visual background.

Receptive field center and directional tuning

We identified an active neurite from a single neuron in the multiphoton field of view (Extended Data Fig. 11a). The RF center of that neurite was identified in real-time and subsequently scanned for directional sensitivity. We developed a custom GUI in MATLAB, which allowed for real-time modifications to stimulus positions on the visual display. This interface enabled hand-triggered looming stimuli and the visual inspection of GCaMP responses. To identify the RF center of an LPLC2 dendritic branch, we created a rectangular grid of 48 positions across the right half of the visual display.

The positions were spaced every 5 LEDs in both horizontal and vertical directions, with each LED covering approximately 2.2° on the retina at the eye's equator. Using the GUI, the experimenter presented a looming stimulus centered at each grid position. The looming stimulus simulated a circular object with a 0.5 cm radius, starting from a distance of 50 cm and traveling at 62.5 cm/s. This caused the object to expand from 0.6° to 14° with a loom velocity (l/v) of 8 ms. If a response was visually detected, the surrounding grid positions were probed next. The position with the highest peak response was taken as the RF center for the subsequent directional tuning experiment. We tested directional selectivity by moving a dark

edge outward from the center of the RF in 24 different directions (Fig. 4g, top; Extended Data Fig. 11). The edges moved at 20°/s with orientations ranging from 0° to 345° in 15° increments. Each edge subtended 15° at the eye's equator and swept 15° orthogonal to its orientation, filling a 15° black square upon completion. Additionally, a looming stimulus centered within the RF, with the same dynamics as those used for the RF scans, was included in this battery of dark moving edges.

LPLC2 position's mapping and directional sensitivity index

We sampled neurons along the DV and AP axes of the lobula and confirmed their anatomical locations by mapping the RF centers onto the fly eye (Fig. 4g, bottom). To identify the putative individual LPLC2 neurons stimulated by the RF center scans, we mapped the horizontal coordinates of their retinal positions onto the 2D retinal ommatidia lattice. We identified specific dorsal and ventral retinal ommatidia and their corresponding columnar LPLC2 in the fly connectome, verifying the recorded LPLC2 neurons' locations (Fig. 4h, Extended Data Fig.11a).

Coordinates were calculated using a 3D reconstruction of the fly head, holder, and visual display in AutoCAD (Autodesk). We estimated the fly ommatidia with overlapping horizontal coordinates through the following steps:

(1) Identified the locations of the ommatidia pointing to positions 16 and 40 based on a Mollweide projection of 3D ommatidia directions from a microCT scan[75];

(2) Mapped these ommatidia locations onto identified visual columns of the male optic lobeconnectome[22];

(3) Used T4 neurons included in these visual columns to identify downstream LPLC2 neurons[22].

For each recording, the direction sensitivity index (DSI) was computed as follows:

$$DSI = (R_{up} - R_{down})/(R_{up} + R_{down})$$

where R_{up} is the peak response to an upward moving edge (0° direction) and R_{down} is the peak response to a downward moving edge (180° direction). The index ranges from -1 to 1, with negative values indicating downward sensitivity and positive values indicating upward sensitivity. The heatmap of the DSI for the tested positions was smoothed with a Gaussian filter (σ = 1).

Imaging data analysis

Images exported from Slidebook 2024 were processed following established protocols[73]. We used a custom MATLAB toolbox developed by Ben J. Hardcastle (available at https://github.com/bjhardcastle/SlidebookObj) to correct for motion artifacts in the x-y plane and to delineate regions of interest (ROI) around individual LPLC2 neurites within the dendritic tree. For each recording, a time-series was generated by calculating the mean fluorescence intensity of pixels within the ROI (Ft) in each frame. These mean values were then normalized to a baseline value using the formula:

$$\Delta F/F = (Ft - F_0)/F_0$$

where F_0 is the mean of Ft during the 0.5 seconds preceding stimulus onset. This approach ensures accurate correction for motion artifacts and reliable quantification of fluorescence intensity changes in LPLC2 neurites.

Statistical analysis of calcium imaging data

Given the repeated sampling and unbalanced sample sizes between groups and conditions, we employed Linear Mixed Effects (LME) models to fit the DSI values. This method maintains statistical power by avoiding averaging procedures and provides more accurate estimates of model parameters, including both fixed and random effects. The fixed effects were defined by the interaction between genotype (control/RNAi) and condition (dorsal/ventral), while the random effects were attributed to individual flies[76,77]. We modeled the data using the R package `**lme4**` assuming residuals followed a Gaussian distribution. Pairwise post-hoc comparisons of the fixed effects were conducted using t-tests with Bonferroni adjustments, implemented through the R package `**emmeans**`. Additionally, to estimate the mean DSI differences across groups and conditions without assuming a specific distribution, we performed standard bootstrap simulations with 10,000 replicates using the R package `**boot**`. Smoothed heatmaps were generated with the R package '**spatstat'**.

Generation of 5xUAS-*DIP-ε*, *-dpr13* and *-beat-VI* transgenic flies

The coding sequences of *DIP-ε*, *dpr13* (isoform RB), and *beat-VI* were cloned into a modified pJFRC5 vector (Addgene: 5XUAS-IVS-mCD8::GFP, plasmid #26218) by replacing the mCD8::GFP coding sequence. Synthesis and cloning were carried out by Genewiz, Inc. Plasmids and sequences are available upon request. Flies were generated by injecting the plasmid into embryos for recombination into attP1 sites (BDSC stock #8621) by BestGene, Inc.

Generation of DIP-ε and dpr13 null alleles

DIP-ε^{null} allele was generated as previously described[78]. Briefly, two sgRNAs were used to generate a frame-shift deletion in the DIP-ε coding sequence. High-score spacer sequences were chosen using the SSC tool[79]. Each sgRNA was cloned into pU6-2-sgRNA-short (Addgene 41700) plasmid and two plasmids were co-injected into vas-Cas9 line (BDSC # 51324) by Bestgene, Inc. Injected larvae were crossed with balancer lines, and PCR-screened in F1 for single flies carrying the deletion. A mutant stock was established from this single F1.
sgRNA target sequence used for *DIP-ε^{null}* allele generation:
DIP-ε^{null} gRNA1: GCTGTTCTGTGGTCATACGATAGC,
DIP-ε^{null} gRNA2: CTTCAATCGATTGACGGTGGAGC

dpr13^{null} allele was similarly generated. SgRNA sequences were identified with an efficiency score above 5, as defined by the CRISPR Efficiency Predictor (https://www.flyrnai.org/evaluateCrispr/). The sgRNA sequence oligos were synthesized (Integrated DNA Technologies) and cloned into the pU6b-sgRNA-short vector[80] to generate a large ~30kb deletion spanning most of the *dpr13* genomic region. All pU6 vectors generated were verified by Sanger sequencing. Two plasmids were co-injected into vas-Cas9 line (BDSC# 51323) in Bestgene, Inc. Injected larvae were crossed with balancer lines, and PCR-screened in F1 for single flies carrying the deletion. A mutant stock lacking the entire coding sequence of *dpr13* was established from this single F1.

sgRNA target sequence used for *dpr13*^{null} allele generation:
dpr13^{null} gRNA1: CGATATAATCCACTTGATGC,
dpr13^{null} gRNA2: ACGTAGCAGCTCCAGGATGT.
Detailed protocols are available upon request.

Immunohistochemistry, tissue clearing and DPX mounting

Brains were dissected in ice-cold Schneider's Drosophila Medium (GIBCO #21720-024) and fixed in PBS containing 4% paraformaldehyde (PFA, Electron Microscopy Sciences 15710) for 30 minutes at room temperature (RT) or in acid-free glyoxal (Addax Biosciences) containing 5% sucrose (Sigma S9378) overnight at 4°C. Brain tissues were washed three times with PBST (PBS containing 0.5% Triton X-100, Sigma T9284) and incubated in blocking solution (PBST containing 10% Normal Goat Serum, Sigma G6767) for at least 1 hour at RT before incubation with the primary antibody. Brains were incubated in primary antibody diluted in blocking solution for two nights at 4°C, washed three times in PBST for 2 hours at RT, then incubated in secondary antibodies diluted in blocking solution for two nights at 4°C. Brains were washed three times in PBST for 2 hours at RT. Subsequent mounting in DPX (EMS 13510) followed the Janelia Adult Drosophila CNS DPX mounting protocol (https://www.janelia.org/project-team/flylight/protocols). After washing from the secondary antibodies, brains were fixed with PBS containing 4% PFA for 30 minutes at RT, rinsed with PBS, and mounted on 22x22mm square No.1.5H cover glass (Thorlabs CG15CH2) previously coated with poly L-Lysine (0.078% solution in deionized water, Sigma P1524) with added 0.2% Kodak Photo-Flo 200 Solution (Electron Microscopy Sciences 74257), followed by a quick 1-2 second rinse with MilliQ water. Brains were dehydrated by placing the cover glass into baths with successively increasing ethanol (Sigma 459844) concentrations (30-50-75-95-100-100-100%, 10 minutes each), followed by three successive baths of xylene (Thermo Fisher Scientific X5-500), 5 minutes each. The glass was uniformly covered with 5-6 drops of DPX (Electron Microscopy Sciences 13510) and placed on a prepared slide between spacers made of two 22x22mm square No.2 cover glasses (Fisher Scientific 12-540B). The slide was left to dry for 24 hours in the hood, then transferred to room temperature and imaged at least 24 hours later.

Antibody information

Primary antibodies and dilutions used in this study: chicken anti-GFP (1:1000, Abcam #13970), rabbit anti-dsRed (1:200, Clontech #632496), mouse anti-Nc82 (1:20, Developmental Studies Hybridoma Bank (DSHB) Nc82), chicken anti-V5 (1:200, Fortis Life Sciences #A190-118A), mouse anti-V5 (1:500, Abcam #27671), rabbit anti-HA (1:200, Cell Signaling Technology #3724), rabbit anti-FLAG (1:200, Abcam #205606), rat anti-N-Cadherin (1:40, DSHB MNCD2), and anti-GFP nanobody (1:200 for expansion microscopy, 1:500 for confocal microscopy, NanoTag Biotechnologies #N0304-At488-L), rat anti-HA (Roche 3F10), 1:500 for expansion microscopy. Secondary antibodies and dilutions used in this study: goat anti-chicken AF488 (1:500, Invitrogen #A11039), goat anti-mouse AF488 (1:500, Invitrogen #A21131), goat anti-mouse IgG2A (1:500, Invitrogen #A21131), goat

anti-rabbit AF568 (1:500, Invitrogen #A11011), goat anti-mouse AF568 (1:500, Thermo Fisher #A11031), goat anti-mouse AF647 (1:500, Jackson ImmunoResearch #115-607-003), goat anti-mouse CF633 (1:500, Biotium #20250-1), and goat anti-rat AF647 (1:500, Jackson ImmunoResearch #112-605-167).

Confocal image acquisition and processing

Immunofluorescence images were acquired using a Zeiss LSM 880 confocal microscope with 488 nm, 561 nm, and 633 nm lasers using Zen digital imaging software with a Plan-Apochromat 63x/1.4 Oil DIC M27 objective. Serial optical sections were obtained from whole-mount brains with a typical resolution of 1024µm × 1024µm, and 0.5µm thick optical sections. Image stacks were exported to either Fiji or Imaris 10.1 (Oxford Instruments) for level adjustment, cropping, removal of off-target brain regions and background noise, and 3D volume reconstructions.

Analysis of neuroanatomical data from image stacks

To measure the axo-dendritic overlap volume between LPLC2 axons and GF dendrites, confocal image stacks of colocalized LPLC2 glomeruli and GF dendrites were imported into Imaris 10.1 for 3D reconstruction using the Surfaces tool to create masks for membranes of pre- and postsynaptic neurons from the corresponding channels. A Surfaces Detail value of 1 micron was used for both LPLC2 and GF surfaces to ensure accurate reconstruction. Background subtraction was applied with a diameter of the largest sphere that fits into the object set to 1 micron to minimize noise and non-specific signals. The overlap volume between the two reconstructed surfaces was then assessed to quantify the spatial relationship between the LPLC2 axons and GF dendrites.

Similar approach was used to measure the overlap between Brp puncta and the GF dendrites in STaR experiments (Extended Data Fig 7), but the number of overlapping reconstructed surfaces was considered regardless of the overlap volume.

To measure LoP4 dendritic branch length in sparsely labeled LPLC2 neurons, corresponding image stacks were imported into Fiji, rotated so that LoP3 and LoP4 branches were seen as antiparallel, and the distance from the point of bifurcation to the most distal tip of the LoP4 branch was measured along Lop4.

Dorsoventral differences in Beat-VI and Dpr13 at the protein level were measured in FIJI. ROIs corresponding to the cell bodies dorsal or ventral LPLC2 clones were drawn manually. Mean Gray Value (average pixel intensity) was used as a proxy of the GFP fluorescence intensity and was measured for two ROIs per sample after background subtraction.

ExLSM and HCR-FISH

Tissue staining, gelation and expansion for ExLSM

Brains were dissected in ice-cold Schneider's Drosophila Medium (GIBCO #21720-024) and fixed in PBS containing 4% paraformaldehyde (PFA, Electron Microscopy Sciences 15710) for 30 minutes on ice. Brains were then washed three

times with PBST (PBS containing 0.5% Triton X-100, Sigma T9284) on ice and left in PBST containing anti-GFP nanobody (NanoTag Biotechnologies #N0304-At488-L) overnight at 4°C. All samples were processed using a protein and RNA retention ExM protocol with minor modifications[81] and adjustments for the fly brain[44]. All solutions used for ExLSM and HCR-FISH were prepared with DNase/RNase free distilled water (Thermo Fisher #10-977-023). After staining, brains were washed three times with PBST on ice and left in MOPS buffer3 (20 mM γ-(N-Morpholino) propanesulfonic acid, Fisher Scientific cat# AC327661000, pH 7.7) containing 1:100 AcX stock solution (acryloyl-X, SE Invitrogen, Cat#A20770 at 10 mg/mL in anhydrous DMSO (Sigma-Aldrich, Cat# 276855)) and 1:2 Melphalan X[82] solution (made by combining 2.5 mg/mL Melphalan, Cayman Chemical Company #16665 with 10 mg/mL AcX overnight shaking at room temperature) overnight at 37°C. Brains were then washed three times with 1xPBS. A gelation chamber was created by applying a Press-to-Seal silicone gasket (Invitrogen, Cat# P24740) to a glass slide, which was then coated with the PLL solution. AcX-treated brains were immobilized on the PLL surface, up to nine per gasket. Gelation solution was prepared just before gelation to prevent premature gel polymerization on ice by adding 10 µL each of 4-hydroxy-TEMPO at 0.5% (w/v) (Sigma-Aldrich, Cat# 176141), TEMED (N,N,N′,N′-Tetramethylethylenediamine at 10% (v/v) (Sigma-Aldrich, Cat# T7024), and ammonium persulfate at 10% (w/v) (Sigma-Aldrich, Cat# A3678) to 470 µL of monomer stock solution (11.5 mL sodium acrylate stock at 4M, prepared by neutralizing 5.5 mL acrylic acid (99% purity; Sigma-Aldrich, Cat# 147230) with 10N NaOH using a water bath and fume hood, in a total volume of 20 mL; 2.5 mL acrylamide stock at 50% (w/v), Sigma-Aldrich, Cat# A9099; 7.5 mL bis-acrylamide stock at 1% (w/v), Sigma-Aldrich, Cat# M7279; 18 mL 5 M NaCl, Sigma-Aldrich, Cat# S5150). Brains were washed with gelation solution, and then the gelation chamber was filled with ~200 µL of gelation solution and incubated on ice for 25 minutes. The gelation chamber was then sealed with a cover slip and placed in a 37°C incubator to gel and cure for 2 hours. Gelation chambers were disassembled, and individual gels were trimmed close to each brain. Gels were trimmed to a right trapezoid shape to ease specimen orientation. Gels were transferred into 12-well plates (Laguna Scientific #4624-12) and incubated with proteinase K (NEB, Cat# P8107S) diluted 1:100 (v/v) in proteinase K digestion buffer (0.5% Triton X-100, 50 mM NaCl, 1 mM EDTA, and 50 mM Tris pH 8) with shaking overnight at room temperature. This resulted in ~2x gel expansion.

HCR-FISH

The HCR-FISH protocol was adapted from Wang et al[82] with minor optimizations for the fly brain[44]. Following digestion with proteinase K, gels with embedded brains were washed 3 times with PBS, transferred into 24-well plates (Laguna Scientific #4624-24), and digested with DNase diluted in RDD buffer (RNase-Free DNase Set, Qiagen #79254) to limit DAPI signal to RNA only and facilitate subsequent analysis for 2 hours at 37°C. After three washes in PBS, gels were equilibrated in Probe Hybridization Buffer (Molecular Instruments, Inc.) for 30 minutes at 37°C, and then transferred to

new 24-well plates containing custom-designed probes (Molecular Instruments, Inc.) diluted in pre-warmed Probe Hybridization Buffer (1 µL of 1 µM stock probe solution per 200 µL of buffer) and left shaking overnight at 37°C. The following day, gels were washed 4 times with pre-warmed Probe Wash Buffer (Molecular Instruments, Inc.) for 20 minutes at 37°C, then washed twice for 5 minutes with SSCT buffer (SSC, Thermo Fisher #AM9763 with 0.05% Triton X-100) at room temperature and transferred to new 24-well plates with HCR Amplification buffer (Molecular Instruments, Inc.) for equilibration. Hairpins (HCR Amplifiers, Molecular Instruments, Inc.) conjugated with AF546 or SeTau647 dyes were diluted in Amplification Buffer (2 µL of each hairpin per 100 µL of buffer), heat-activated in a thermal cycler (90 seconds at 95°C), removed, and kept for 30 minutes at room temperature in the dark. After 30 minutes, the hairpins were added to the 24-well plates with gels (300 µL per well) and incubated with shaking at room temperature in the dark for 3 hours. The hairpin solution was then removed, and the gels were washed 4 times with SSCT and 2 times with SSC for 10 minutes at RT in the dark. Gels were subsequently stored at 4°C in SSC until final expansion.

Sample mounting

Samples were expanded to ~3X in 0.5x PBS containing 1:1000 SYTO-DAPI (Thermo Fisher S11352) at room temperature for 2 hours before mounting onto PLL-coated coverslips (see description for DPX mounting above). The coverslips were then bonded with Bondic UV-curing adhesive (Bondic starter kit, Bondic) onto a custom fabricated sample holder (Janelia Tech ID 2021-021) to be suspended vertically in the imaging chamber. Mounted samples were imaged in 0.5x PBS with 1:10,000 SYTO-DAPI after a minimum of 1 hour of equilibration in the imaging chamber. Unexpanded gels were stored at 4°C in 1X PBS + 0.02% sodium azide (Sigma-Aldrich, Cat# S8032) for up to 14 days before final expansion and imaging.

Light-sheet microscopy

Images were acquired on a Zeiss LS7 microscope equipped with 405 nm, 488 nm, 561 nm, and 638 nm lasers. Illumination optics with a 10x/0.2 NA were used for excitation (Zeiss, Cat# 400900-9020-000). Detection was performed using a W Plan-Apochromat 20x/1.0 DIC M27 water immersion objective (Zeiss, Cat# 421452-9700-000). The LS7 optical zoom was set to 2.5x, resulting in a total magnification of 50x. DAPI and AF546 dyes were simultaneously excited by the 405 nm and 561 nm laser lines, and emission light was separated by a dichroic mirror SBS LP 510 with emission filters BP 420-470 (Zeiss, Cat# 404900-9312-000) and a modified BP 527/23 (Chroma, Cat# ET672/23m). Similarly, AF488 and SeTau647 dyes were simultaneously excited via 488 nm and 638 nm, and the emission was split through a dichroic SBS LP 560 with emission filters BP 505-545 and LP 660 (Zeiss, Cat# 404900-9318-000). To eliminate laser transmission, a 405/488/561/640 laser blocking filter (Zeiss, Cat# 404900-9101-000) was added to the emission path. Images were captured using dual PCO.edge 4.2 detection

modules (Zeiss, Cat# 400100-9060-000) with a 50 msec exposure time. Filter and camera alignment were manually calibrated prior to each imaging session. Image volumes were acquired at optimal Z-step and light-sheet thickness, and the Pivot Scan feature was used to reduce illumination artifacts by sweeping the light-sheet in the xy-plane. The LS7 microscope was operated using ZEN Black 3.1 (v9.3.6.393).

Analysis of HCR-FISH data from ExLSM Image Stacks

The full details of our analysis are available in our previous publication[45]. The acquired z-stacks, stored in CZI format, were imported and pre-processed to remove noise and artifacts generated by the imaging modality. These artifacts included limited channel contrast, variations in contrast from image to image within a dataset, background noise fluctuations due to both intra-channel variations and inter-channel crosstalk, and localized brightness changes from varying fluorophore concentrations within and among stained nuclei. Pre-processing involved the following steps: full-scale contrast stretching (FSCS) to normalize luminosity across different channels, local background removal using a 3D Gaussian filter, a second FSCS to adjust for any contrast loss due to background removal, and a final median filter to remove any remaining localized noise. These pre-processed stacks served as the starting point for instance segmentation of the nuclei. First, the nuclei centers were identified using a Laplacian-of-Gaussian (LoG) filter. Then, the imaged volume was subdivided into 3D Voronoi cells, using the detected centers as seeds and Euclidean distance. Each cell contained one nucleus, which was segmented using a threshold obtained by minimizing an energy functional designed to find the optimal surface separating the nucleus from the surrounding cytoplasm. Once each nucleus was segmented, the FISH puncta were identified within the 3D volume associated with it using a LoG filter, and only the puncta within the nucleus region and its immediate surrounding volume were counted. Pre-processed products, segmented nuclei features, associated FISH puncta, and their features were stored for further analysis. Puncta counts were normalized by the maximum count for each brain. The significance of gene expression relationships inferred from HCR-FISH (Fig. 2) was assessed using both a linear regression model and a multi-level negative binomial generalized linear mixed model, accounting for inter-animal heterogeneity: random effects were attributed to individual animals (Supplemental Table 2). The package was written in Python, is open-source, and available for download at https://github.com/avaccari/DrosophilaFISH.

Genetic Intersection of cell types and genes

To assess gene expression levels within LPLC2 and LPLC1 cell types, we used a combination of GAL4 and LexA binary expression systems. Expression of a LexAop-FRT-stop-FRT-membrane marker controlled by a cell-type-specific LexA driver was blocked until the FRT-stop-FRT cassette was excised by a Flippase, driven by a gene-specific T2A-GAL4 driver line[83]. Additionally, an unconditional membrane marker controlled by the same LexA driver visualized the entire cell population. The list of fly stocks used is available in Supplemental Table 1.

Sparse labeling of neuronal populations

To visualize single cell morphology of LPLC2 dendrites in the lobula plate (Fig 4) and for dorsoventral HCR-FISH analysis (Ext. Data Fig. 4), we used MultiColor FlpOut (MCFO)[84], a genetic tool for sparse labeling individual cells within a neuronal population acting downstream of a given GAL4 driver. 24h old pupae were heat shocked in a 37°C water bath for ten minutes to achieve the labeling of one LPLC2 neuron per hemibrain om average.

Analysis of the Flywire Connectome reconstruction

To analyze the *Flywire* connectome, we developed an open-source Python package, available at https://github.com/avaccari/DrosophilaCon. The primary library used by *DrosophilaCon* to interface with the *FlyWire* connectome is *fafbseg*[32,34] (version 3.0.0). This package enables users to specify the labels of "source" and "target" neurons and generates a connectivity diagram where target neurons are color-coded based on the total count of synapses with the source neurons. Once the labels are specified, the package queries the latest available annotations to identify all neurons matching (or containing) the labels. The primary sources of annotation used to identify the neurons are:
(1) Free-form community annotations provided through the *neuroglancer* user interface (https://github.com/google/neuroglancer).
(2) Systematic annotations for the entire brain[34].
(3) Systematic cell types for the right optic lobe[85].
Next, the latest version of the *FlyWire* production dataset is queried for the adjacency matrix representing the connectivity between each neuron in the source and each neuron in the target for the selected side of the brain. This information is returned as an adjacency table, providing the counts of synapses between each source-target pair. There are two versions of the synapse datasets: one filtered by synaptic cleft and one unfiltered. We used the unfiltered dataset because the filtered version applied a fixed threshold for distance, resulting in reduced synapse counts. The adjacency table was used to evaluate the total synapse counts for each target neuron. These counts were normalized by the maximum count observed across all target neurons. The mesh representation for each identified target neuron was downloaded from the *FlyWire* dataset, skeletonized to optimize processing, and displayed with color-coding corresponding to the normalized synapse count, allowing for comparison across different source-target pairs.

Statistical analysis

All statistical analyses were performed using RStudio 1.4.1103, MATLAB, or Prism 9.2.0 (GraphPad). Significance levels were defined as follows: $p < 0.05$, $*p < 0.01$, $**p < 0.001$, $***p < 0.0001$ for all figures. Statistical tests were chosen based on data distribution, which was assessed using the Kolmogorov-Smirnov test in R with a p-value threshold of <0.05 for normality. Two groups of normally distributed data sets were tested for statistically significant differences using unpaired t-tests with Welch's correction for non-identical variance. For comparisons involving more than two groups, we employed either one-way

ANOVA followed by Tukey's HSD test for post-hoc pairwise comparisons or the Kruskal-Wallis test followed by Dunn's multiple comparisons post-hoc test with Bonferroni correction. Binary data were compared using chi-squared tests. Detailed statistical analyses for behavioral data, HCR-FISH data, and neuroanatomical data are described in Supplementary Table 2. All other statistical tests, number of replicates, significance levels, and other elements of the statistical analysis are reported within the corresponding Methods and Results sections and/or Figure Legends. No data were excluded from the analysis unless specified in the corresponding Methods section. All measurements were taken from distinct samples.

Data availability

The datasets generated and/or analyzed during the current study are available from the corresponding authors upon reasonable request. For further information regarding any resources and reagents, please contact S. Lawrence Zipursky (lzipursky@mednet.ucla.edu) and Gwyneth M. Card (gc3017@columbia.edu). Source Data are provided with this paper.

Code availability

The code for single-cell RNA-seq analysis is available at https://github.com/kurmangaliyev-lab. Our code for the analysis of Flywire and "hemibrain" connectome reconstructions is available at https://github.com/avaccari/DrosophilaCon and https://github.com/avaccari/DrosophilaVPNWiring, respectively. Code used to analyze HCR-FISH data is available at https://github.com/avaccari/DrosophilaFISH. Code related to calcium imaging experiments is available at https://osf.io/z7xfk/. All other code can be made available from the corresponding authors upon request.

Acknowledgements

We thank the Bloomington Stock Center (NIH P40OD018537), Vienna *Drosophila* Research Center and Janelia Fly Facility for providing fly stocks. We also thank the UCLA BSCRC Sequencing Core and the UCLA TCGB core for help with library preparation and scRNA-seq; the UCLA BSCRC FACS core for assistance with FACS purification. We thank members of the Flywire Consortium for connectome annotation in the FAFB dataset. We thank all members of the Zipursky lab for advice and comments on the manuscript. This work was supported by the HHMI-Helen Hay Whitney Foundation (M.D.), NEI K99EY036123 (M.D.), NEI R01EY026031 (M.F.), and NINDS R01NS118562 (C.R.v.R) S. L. Z. and G.M.C. are investigators of the Howard Hughes Medical Institute.

Author Contributions

Conceptualization and Methodology: M.D., Y.Z.K, C.R.v.R., M.A.F., G.M.C., S.L.Z.; Investigation & Data collection: M.D., Y.Z., G.F., H.J., Parmis S. Mirshahidi, A.R., R.H.H., C.L., A.M. and Pegah S. Mirshahidi; Data analysis: M.D., Y.Z.K.,

A.V., Y.Z., G.F., H.J., F.X., B.W.H.; Writing and editing.; M.D., Y.Z.K., Y.Z., G.F., H.J., P.S., C.R.v.R., G.M.C. and S.L.Z.; Supervision and funding acquisition: S.L.Z, G.M.C., C.R.v.R., M.A.F., M.D.

Ethics Declarations

Competing interests

The authors declare no competing interests

Figure 1

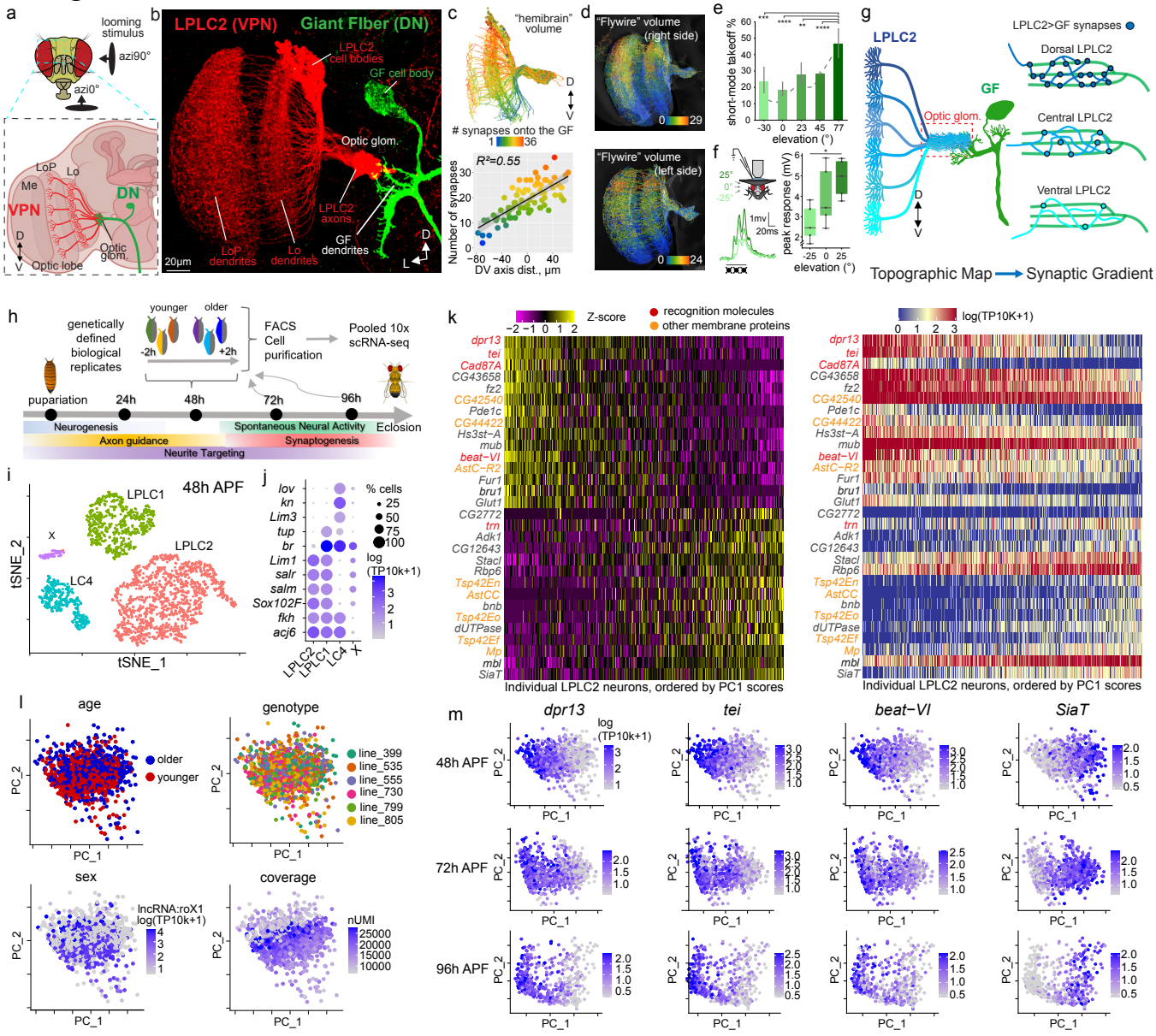

Figure Legends

Fig. 1: Gradients of recognition molecules correlate with synaptic gradients and behavior in Visual Projection Neurons

a-d, Anatomy

a, Visual Projection Neurons (VPN) have dendrites that cover the lobula (Lo), lobula plate (LoP) or both neuropils of the fly optic lobe. Axons converge on optic glomeruli in the central brain innervated by dendrites of target neurons, e.g., Descending Neurons (DN); D-dorsal, V-ventral, L-lateral.

b, Confocal projection (posterior view) of LPLC2 VPNs and the GF.

c, Top: EM-based reconstructions of LPLC2 neurons (posterior view) from the "hemibrain" volume, color-coded to indicate the number of synapses each LPLC2 axon forms with the GF. Bottom: linear regression of LPLC2-GF synapse numbers as a function of LPLC2 dendrite position along the DV axis of the visual space. Dots, individual LPLC2 neurons (colored as above). Shaded region, 95% confidence interval).

d, same as (**c**, top), inferred from the Flywire volume (left and right sides)

e, **Behavior**: GF-mediated short-mode (<7 ms sequence duration) takeoffs in response to lateral (90°) looms at various elevations. Error bars, 95% confidence intervals.

f, **Electrophysiology**: left, schematic representation and averaged responses of the GF to looming stimuli at different elevations. The line below the traces indicates the duration of the expansion of the looming disks. Right, pooled mean of peak responses for GF in response to looming stimuli at different elevations across five repeated trials. Each dot represents a single fly.

g, **Summary**: Transformation of retinotopic dendritic maps into axonal synaptic gradients between LPLC2 and the GF without axonal retinotopy.

h-m, **Identification of gene expression gradients in VPNs**.

h, Single-cell RNA-sequencing experimental design (See Methods).

i-i, t-SNE plots of 48h APF dataset (**i**) LPLC2, LPLC1, and LC4 neurons were annotated based on the expression of known marker genes (**j**). X, unknown ectopic cell type.

k, Heatmaps of the expression patterns of the top 30 genes with the highest contribution (loading) to Principal Component 1 (PC1, 15% variance explained) across LPLC2 neurons at 48h APF (PCA was performed separately on LPLC2 neurons); genes (rows) ordered by their loadings to PC1; cells (columns) ordered by their PC1 scores; expression patterns colored by scaled expression levels (left) and original log-normalized expression values (right).

l, Distributions of LPLC2 neurons at 48h APF along PC1 and PC2 (PCA plots) colored by developmental age, genotype, sex (male-specific transcript), and coverage.

m, PCA plots of LPLC2 neurons at 48, 72, and 96h APF, colored by the expression levels of the select genes from (**k**). Differential expression of these genes is consistent over time.

Figure 2

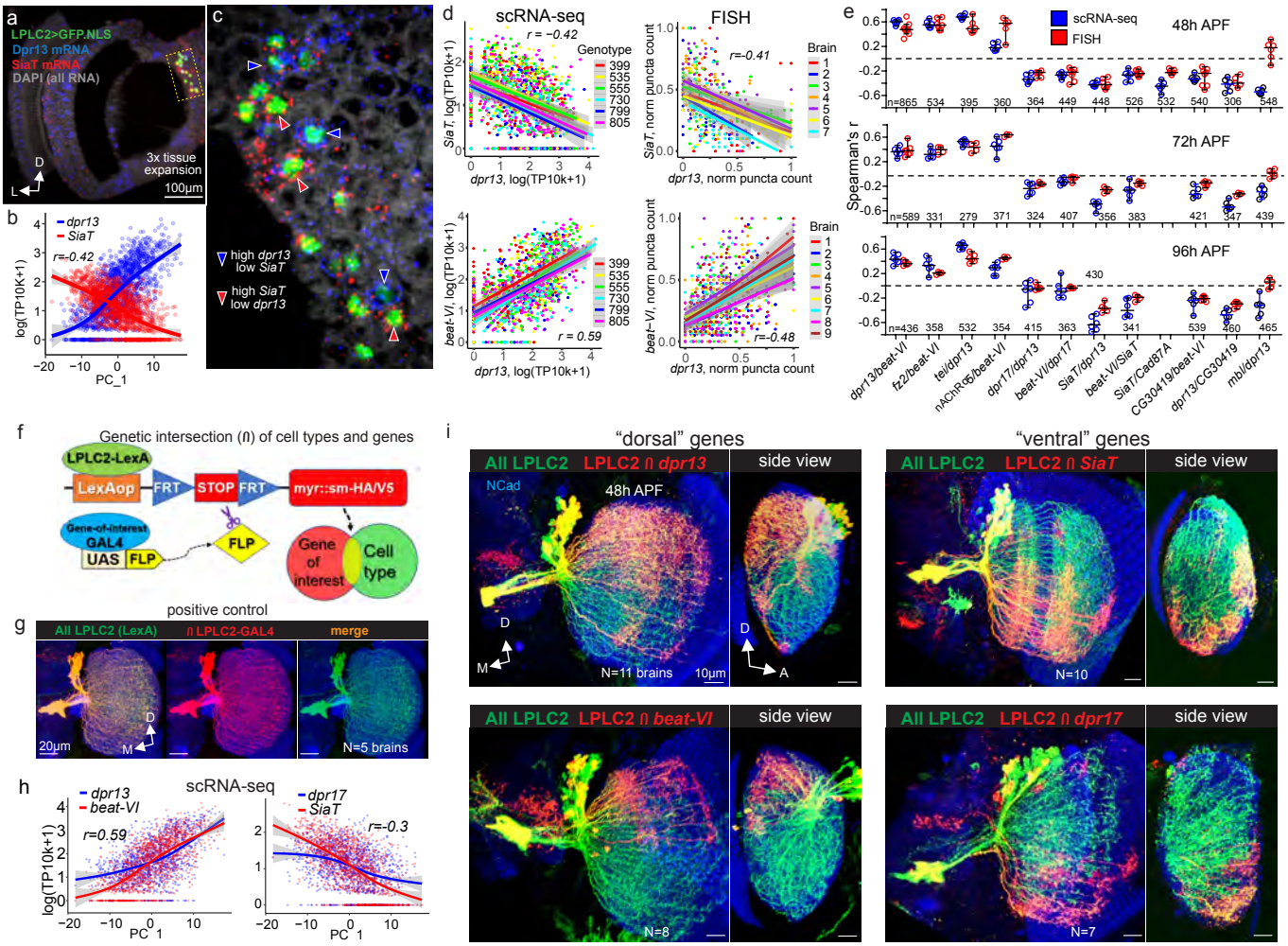

Fig. 2: Gradients of recognition molecules align with synaptic gradients

a-e, FISH analysis.

a, Light sheet projection of the expanded *Drosophila* optic lobe (48h APF) with labeled LPLC2 nuclei and transcripts of *dpr13* and SiaT.

b, Anti-parallel expression of *dpr13* and *SiaT* across LPLC2 neurons at 48h APF (inferred from scRNAseq, along PC1). Fitted lines, trends of gene expression changes along PC1; shaded areas, 95% confidence intervals. r, Spearman's rank correlation coefficient.

c, Single slice (0.5µm thick) from the projection in (**a**) (zoomed into the dashed rectangular region); arrows indicate individual LPLC2 neurons expressing markedly different levels of *dpr13* and *SiaT*.

d, Comparison of scRNA-seq (left) and FISH (right) measuring correlation in expression for two pairs of graded genes: *dpr13/SiaT* (top) and *dpr13/beat-VI* (bottom) across LPLC2 neurons at 48h APF. Fitted lines, linear relationship between the expression levels of two genes for each brain (FISH) or each wild-type genotype (scRNA-seq). Shaded regions, 95% confidence intervals.

e, Comparison of RNA-seq and HCR-FISH measuring correlation in expression for twelve pairs of genes at three time points across LPLC2 neurons. Individual dots represent Spearman's rank correlation coefficients for each brain (FISH) and each genotype (scRNA-seq). Error bars, means ±95% confidence intervals; n, total number of neurons tested using FISH.

f-i, GAL4-reporter analysis.

f, Genetic approach to visualize a subset of neurons within a VPN cell type population expressing a specific gene at a particular time point.

g, Positive control for (**f**). LPLC2-LexA genetically intersected with LPLC2-GAL4, results in labeling of all LPLC2 neurons.

h, Correlation between expression levels of *dpr13/beat-VI* and *dpr17/SiaT* (inferred from scRNA-seq), along PC1 across the LPLC2 population at 48h APF.

i, Subsets of LPLC2 neurons expressing *dpr13*, *dpr17*, *beat-VI* and *SiaT* at 48h APF. D, dorsal; M, medial; A, anterior.

Figure 3

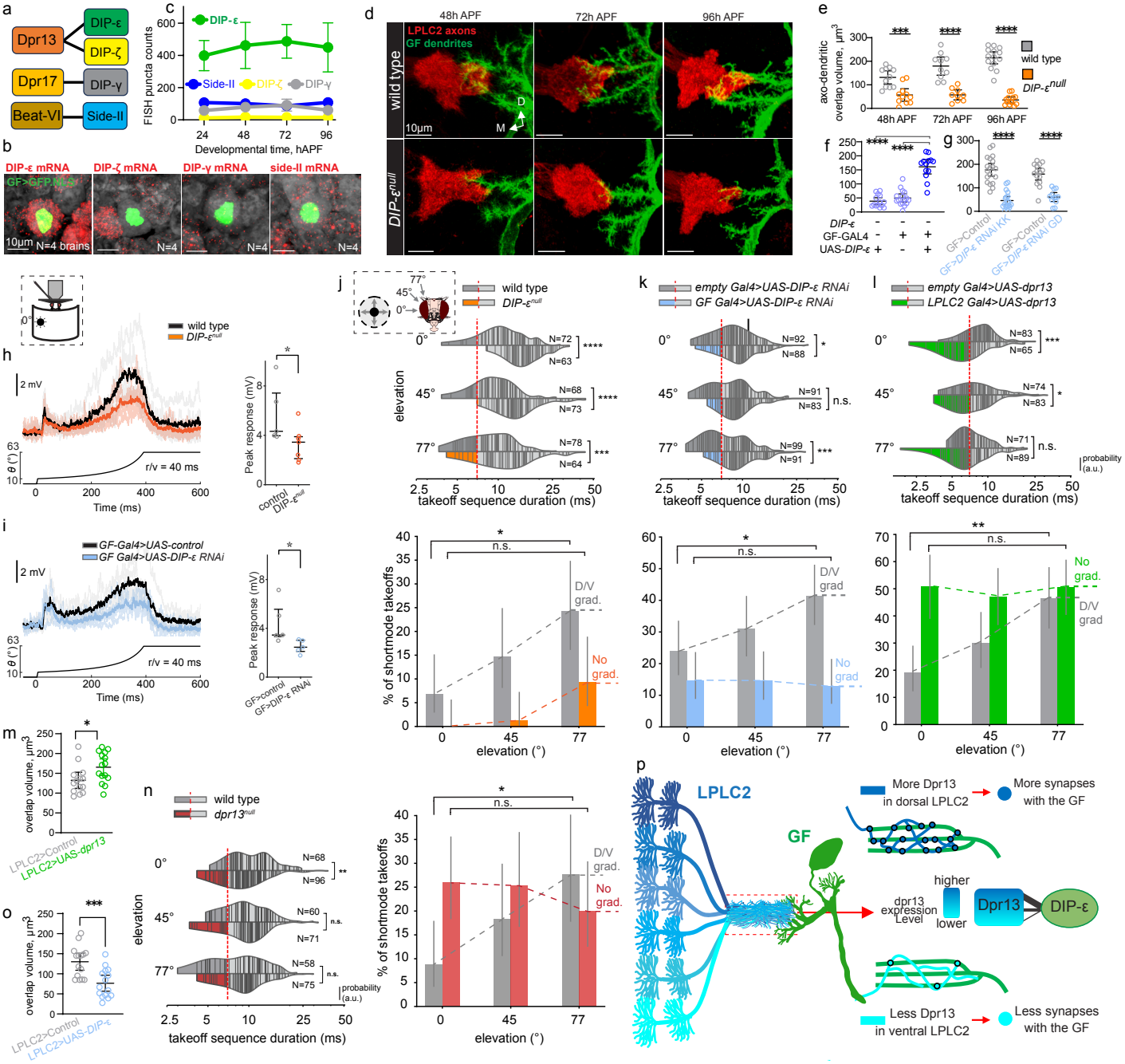

Fig. 3: A gradient of DIP-ε::Dpr13 recognition molecules controls a looming escape synaptic gradient in LPLC2 neurons

a, Protein interaction map showing molecular binding partners of most differentially expressed recognition molecules in LPLC2.

b, Light sheet projections of the GF (nuclear marker). Red puncta, mRNA of designated genes assessed through HCR-FISH.

c, Candidate gene expression levels (FISH puncta counts) in the GF throughout development. Error bars, means with ±95% confidence intervals.

d, Confocal projections of LPLC2 axon terminals and the GF dendrites in wild type and *DIP-ε^{null}* animals throughout development. M, medial; D, dorsal.

e-g, Comparison of LPLC2-GF axo-dendritic overlap volume (see Methods) between controls and in *DIP-ε^{null}* animals (**e**), DIP-ε rescue in the GF (**f**), and GF expressing two different DIP-ε RNAi (**g**).

h, Whole-cell patch-clamp recordings in the GF during presentations of looming stimuli. Left: GF responses to looming stimuli, r/v = 40ms. Control (average: black, individual fly: grey) and *DIP-ε^{null}* (average: orange, individual fly: light orange) traces are overlayed. Looming stimulus profile over time is displayed below the GF responses. Right: Quantification of expansion peak amplitudes from individual flies; each data point represents the mean value of two recordings per animal.

i, Same as (**h**) for controls (grey) and animals overexpressing DIP-ε RNAi in the GF (light blue).

j, Top: Violin plots of takeoff sequence durations for lateral stimuli (90°) at different elevations (0°, 45°, 77°) in wild-type and *DIP-ε^{null}* animals. Lines, single takeoffs. Short-mode (<7 ms, grey for wild-type, orange for *DIP-ε^{null}*) and long-mode (≥7 ms, grey) durations separated by a red dashed line. N = number of flies. Bottom: short-mode takeoff percentages at different elevations. Error bars, 95% confidence intervals. Dashed lines, wild-type DV gradient (grey) and eliminated DV gradient in *DIP-ε^{null}* (orange).

k, Same as (**j**) for controls (grey) and animals overexpressing DIP-ε RNAi in the GF (light blue).

l, Same as (**j**) for controls (grey) and animals overexpressing *dpr13* in LPLC2 neurons (green).

m, Comparison of LPLC2-GF axo-dendritic overlap volume in control animals, and animals expressing overexpressing *dpr13* in LPLC2.

n, Same as (**j**) for wild-type (grey) and *dpr13^{null}* animals (red).

o, Same as (**m**), for control animals, and animals overexpressing DIP-ε in LPLC2.

p, Suggested model: a dorsoventral gradient of Dpr13 across the population of LPLC2 neurons determines the number of synapses each LPLC2 axon makes with the GF via binding with DIP-ε on the GF dendrites.

panels **e**, **f**, **g**, **m**, **o**: dots, individual brains. Error bars, means ±95% confidence intervals.

Figure 4

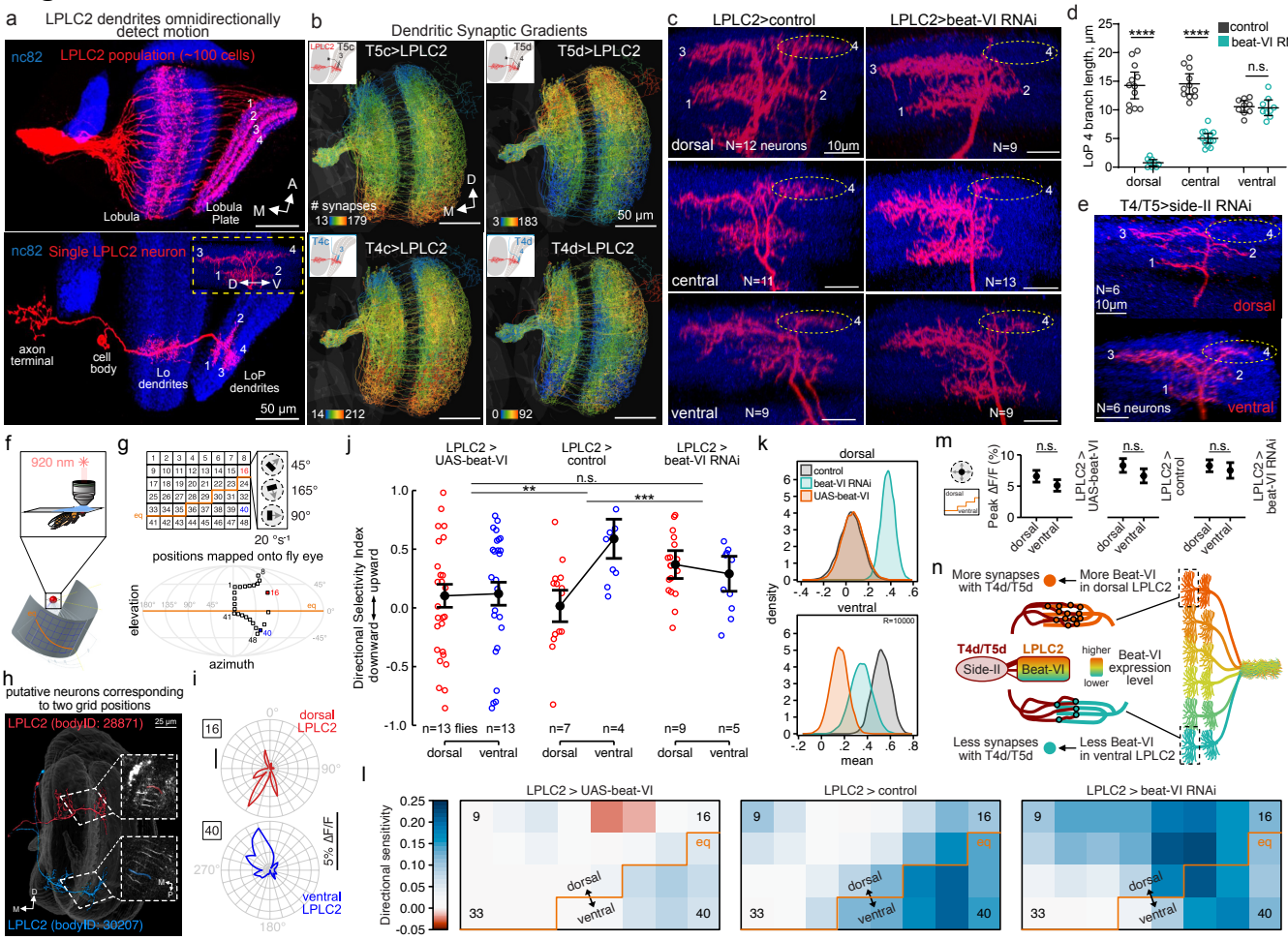

Fig. 4: A gradient of Beat-VI::Side-II recognition molecules controls a motion detection synaptic gradient in LPLC2 neurons

a-b, LPLC2 dendritic synaptic gradients

a, Confocal projections of the LPLC2 population (top) and an individual LPLC2 neuron (bottom) in dorsal view, highlighting the dendritic branches in the lobula plate (LoP). Numbers, LoP layers. Inset: posterior view of a single LPLC2 LoP dendrite with branches extending into only one of the four cardinal directions in each layer. D, dorsal; V, ventral; M, medial; P, posterior.

b, EM-based reconstructions (Flywire connectome) of LPLC2 neurons (posterior view), color-coded by the number of inputs each LPLC2 neuron receives from T4c, T4d, T5c and T5d neurons. Insets, schematics of single LPLC2 (red) and T4/T5c-d neurons, overlaid on lobula/lobula plate outlines.

c-e, Beat-VI differentially regulates LPLC2 dendrite morphology along the LoP4 DV axis.

c, Confocal projections of individual LoP dendrites (posterior view) in dorsal, central and ventral LPLC2 in control and LPLC2>*beat-VI* RNAi flies. Numbers, LoP layers. Dashed ovals, LoP4 dendritic branches.

d, Length of LoP4 dendritic branches for dorsal, central and ventral LPLC2 neurons in control and LPLC2>*beat-VI* RNAi flies. Dots, individual neurons. Error bars, means ±95% confidence intervals.

e, Confocal projections of individual LoP dendrites (posterior view) of dorsal and ventral LPLC2 neurons in control and T4/T5>*side-II* RNAi flies. Dashed ovals, LoP4 dendritic branches.

f-n, Beat-VI differentially regulates integration of motion by LPLC2 neurons

f, Schematic of the fly eye relative to the surrounding LED display for visual stimulation during two-photon calcium imaging.

g, Positions on the LED display probing LPLC2 receptive field by presentation of dark edges moving in 24 (0° to 345°) different orientations (top). Yellow line, fly eye's equator (eq) projected onto the LED display. Mollweide projection of the outermost positions (black boxes) relative to the fly eye during Ca2+ imaging experiments (bottom).

h, EM-based reconstructions of LPLC2 neurons stimulated by grid positions 16 and 40 (see Methods). LPLC2 neurites viewed during Ca^{2+} imaging with single-cell regions of interest (color-coded by positions) overlaid on them (insets, scale bar: 10 μm).

i, Polar plots of the peak responses to moving dark edges in dorsal and ventral LPLC2 neurons in a representative fly.

j, Directional sensitivity index (DSI) for dorsal and ventral LPLC2 neurons in control, *beat-VI* RNAi, and UAS-*beat-VI* flies. Dots, individual recordings. Error bars, means ±95% confidence intervals. Black lines, interactions between positions and genotypes

k, Bootstrap of the mean of the DSI in dorsal (16, top)) and ventral (40, bottom) regions for control, *beat-VI* RNAi, and UAS-*beat-VI* flies (10,000 repetitions).

l, Average peak responses to a looming stimulus above (dorsal) or below (ventral) the eye's equator in control *beat-VI* RNAi, and UAS-*beat-VI* flies. Error bars, means ±95% confidence intervals.

m, Filtered heatmap of the DSI for all positions tested in control, *beat-VI* RNAi, and UAS-*beat-VI* flies.
n, Suggested model: a dorsoventral gradient of Beat-VI across the population of LPLC2 neurons determines the number of synapses each LPLC2 dendrite makes with T4d/T5d neurons via binding with Side-II on T4d/T5d axons.

Extended Data Figure 1 (related to Fig. 1)

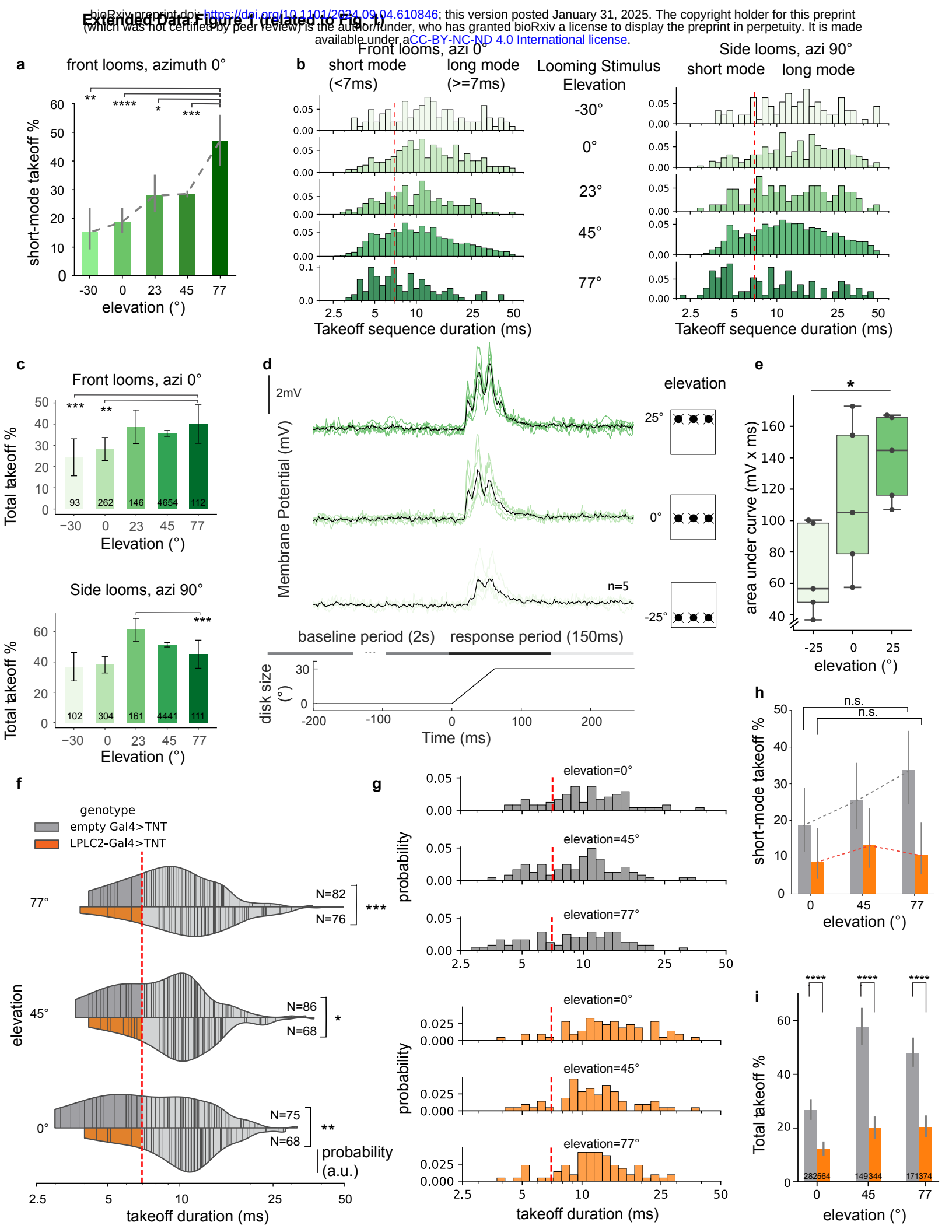

Extended Data Figure 1 (related to Fig. 1). LPLC2-GF dorsoventral synaptic gradient biases the looming escape circuit towards short-mode takeoffs at higher stimulus elevations.

a, GF-mediated short-mode (<7 ms sequence duration) takeoffs in response to frontal (0°) looms at various elevations. Error bars, 95% confidence intervals.

b, Histograms showing the distribution of takeoff sequence durations in response to frontal (left) and lateral (right) looming stimuli at different elevations (detailed breakdown of data summarized in Fig. 1e). Short-mode (<7ms) and long-mode (≥7ms) takeoffs are distinguished by the red dashed lines.

c, Total takeoffs in response to frontal (0°) and lateral (90°) looms at various elevations. Error bars, 95% confidence intervals.

d, Top: whole-cell electrophysiological recordings of the GF in response to looming stimuli at different elevations in control animals. Black traces represent averaged responses of five animals, green traces represent responses of individual animals. Middle: baseline region (2s before the onset of stimulus) and response region (150ms after the onset of stimulus) defined in the traces for analysis of GF responses. Bottom: change of disk size over time.

e, Pooled mean of integrated potentials for GF in response to looming stimuli at different elevations across five repeated trials. Each dot represents a single fly.

f, Violin plots of takeoff sequence durations for lateral stimuli (90°) at different elevations (0°, 45°, 77°) in controls and LPLC2-silenced animals. Lines, single takeoffs. Short-mode and long-mode durations are separated by a red dashed line. N = number of flies.

g, Short-mode takeoff percentages at different elevations for controls and LPLC2-silenced animals. Error bars, 95% confidence intervals. Dashed lines indicated gradient trends.

h, Histograms showing the distribution of takeoff sequence durations in response to lateral looming stimuli at different elevations in controls and LPLC2-silenced animals (detailed breakdown of in **f**-**g**). Short-mode and long-mode takeoffs are distinguished by the red dashed lines.

i, Total takeoff percentages at different elevations for controls and LPLC2-silenced animals. Error bars, 95% confidence intervals.

Extended Data Figure 2 (related to Fig. 1)

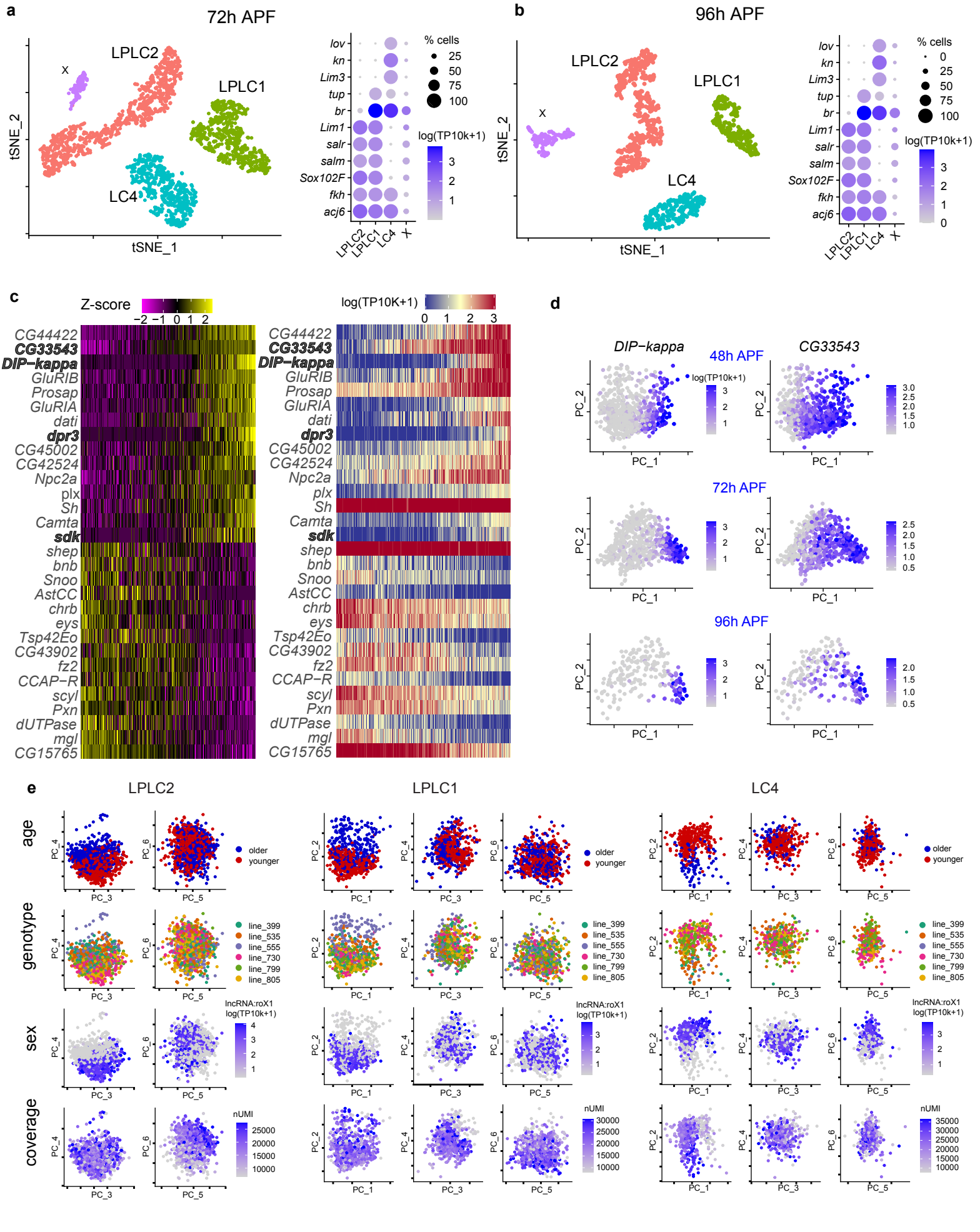

Extended Data Figure 2 (related to Fig. 1).
Synaptic gradients are associated with molecular heterogeneity across VPN cell types

a-b, t-SNE plots of 72h APF (**a**) and 96h APF (**b**) datasets. LPLC2, LPLC1, and LC4 neurons were annotated based on the expression of known transcription factors (right panels). X indicates unknown ectopic cell types.

c, Heatmaps of the expression patterns of the top 30 genes with the highest contribution (loading) to differentially expressed genes along Principal Component 1 (PC1, 15.2% variance explained) across LPLC1 neurons at 48h APF (see Fig. 1 legend for details). Genes encoding cell recognition molecules (IgSF superfamily) are highlighted in bold.

d, PCA plots of LPLC1 neurons at 48, 72, and 96h APF, colored by the expression levels of two cell recognition molecules from (**c**).

e, PCA plots of LPLC2, LPLC1, and LC4 neurons at 48h APF colored by genotype, age (early vs late collection), genotype (DGRP line), sex (male-specific transcript), and coverage. PC1-6 for LPLC1 and LC4, and PC3-6 for LPLC2 are shown.

Extended Data Figure 3 (related to Fig. 1)

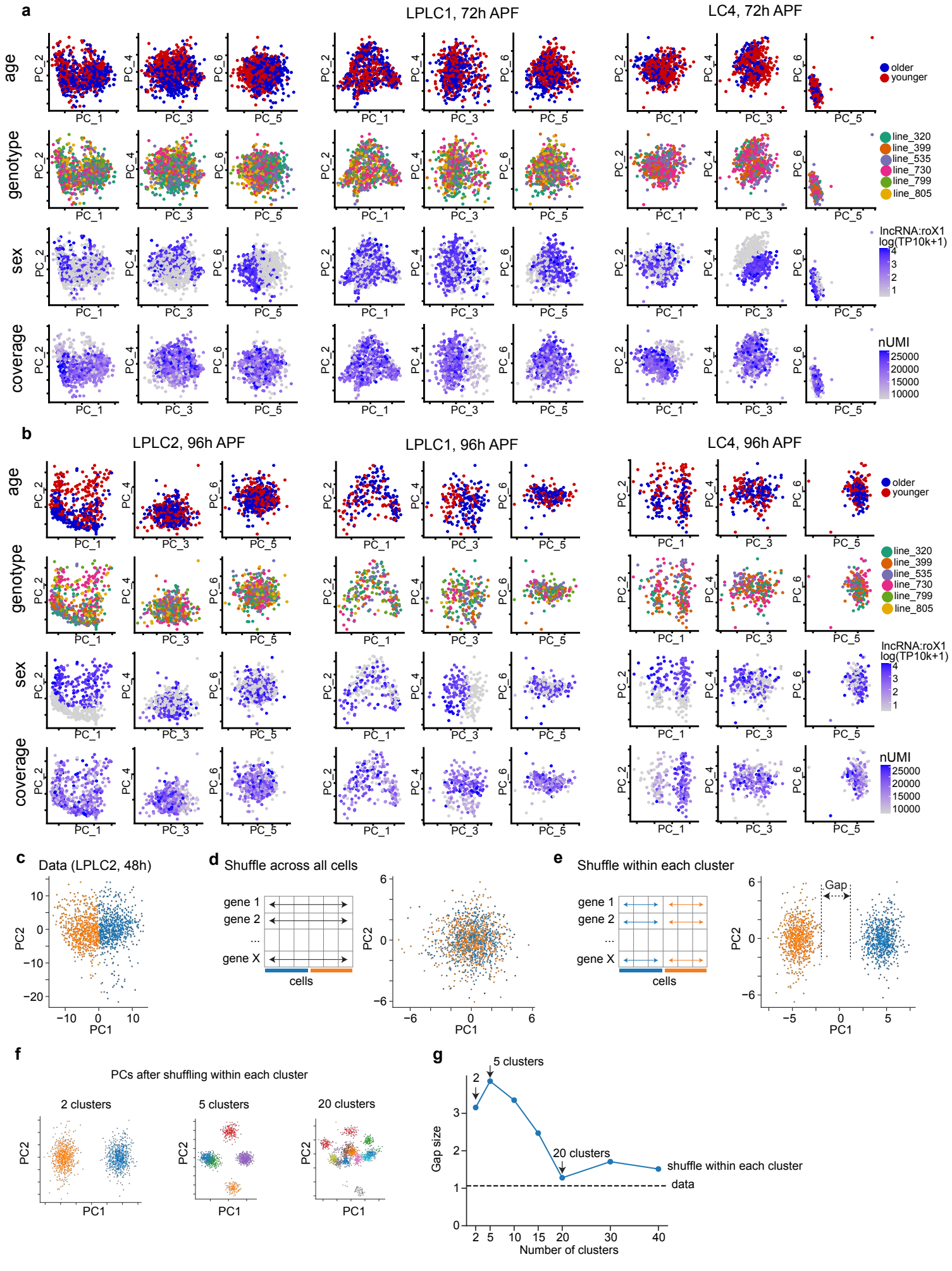

Extended Data Figure 3 (related to Fig. 1). Further analysis of within-cell-type heterogeneity in gene expression across LPLC2, LPLC1 and LC4

a-b, PCA plots of LPLC2, LPLC1 and LC4 neurons at 72h APF (**a**) and 96h APF (**b**) colored by genotype, age (early vs late collection), genotype (DGRP line), sex (male-specific transcript), and coverage. Shown are PC1-6. Variance explained by PC1 at 72h: 32% for LPLC2, 17% for LPLC1, 11% for LC4. Variance explained by PC1 at 96h: 28% for LPLC2, 15% for LPLC1, 21% for LC4.

c-e, Scatter plots of LPLC2 cells (48h APF) embedded in the first two principal components (PC1 and PC2) colored by their cluster labels (n=2, inferred from K-means clustering). PCs are calculated using the top 1000 highly variable genes based on the actual data (**c**), after shuffling gene expression levels for each gene independently across all cells (**d**), and after shuffling each gene only within each cluster (**e**), respectively. Shuffling gene expression across all cells (**d**) disrupts this gradient, indicating that the observed differences reflect coordinated gene expression rather than uncorrelated variation. Shuffling within each cluster (**e**) disrupts the internal gradient of each cluster, creating artificial gaps not present in the original data (**c**), which suggests that the continuous gradient observed in the original data cannot be represented as a set of discrete clusters.

f, Scatter plots of cells in PCA embeddings after shuffling genes within each cluster for an increasing number of fine-grained clusters (n=2,5,30).

g, Gap size as a function of the number of clusters. Gap size is defined as the minimum distance in PC1 and PC2 space needed to connect 90% of cells into a single graph component. The gap size decreases and plateaus as the number of clusters increases. This means that a continuum can be approximated by a large number of discrete clusters. However, a small number of clusters (like 2) is insufficient to capture the continuous nature of the data.

Extended Data Figure 4 (related to Fig. 2)

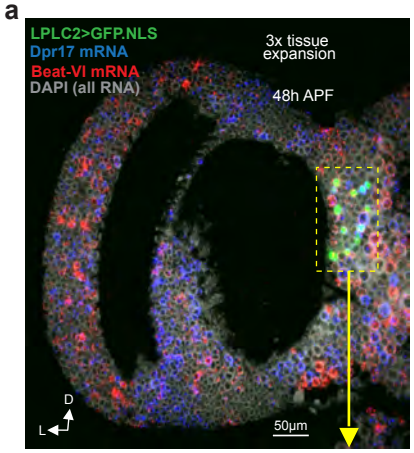

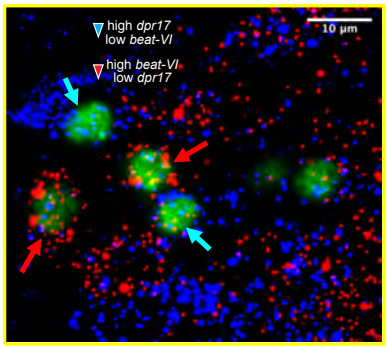

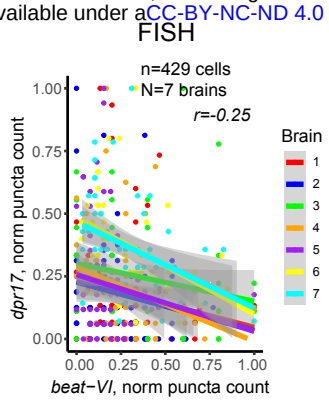

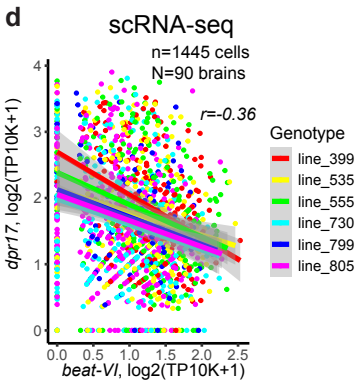

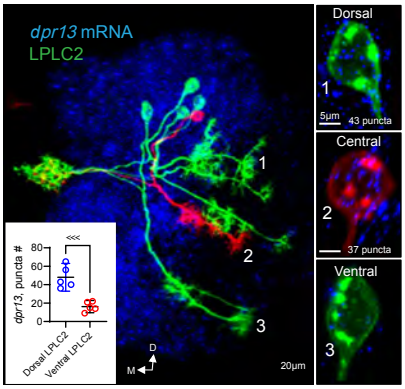

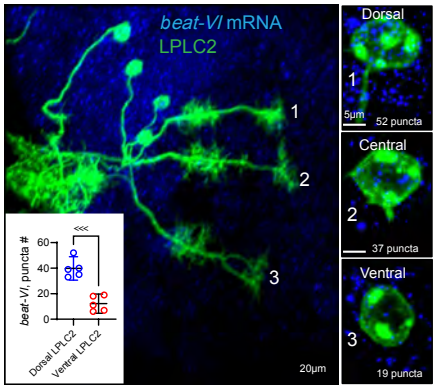

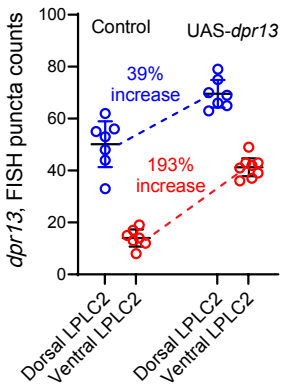

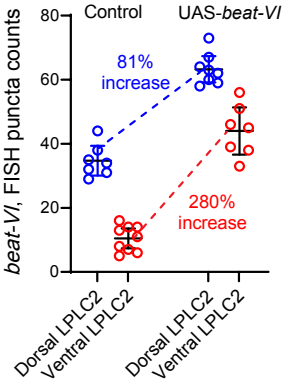

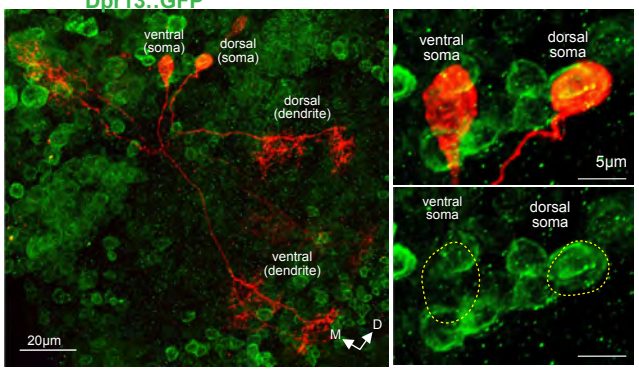

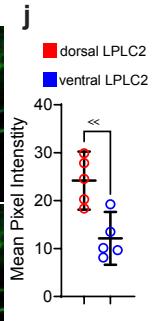

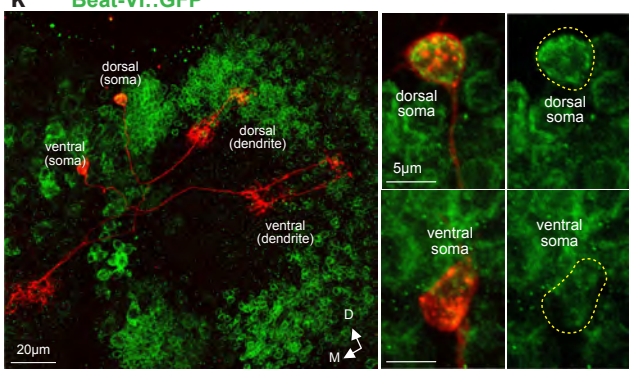

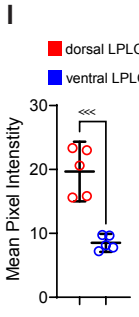

Extended Data Figure 4 (related to Fig. 2). Molecular validation of graded gene expression in LPLC2.

a-b, Light sheet projection of the expanded *Drosophila* optic lobe (48h APF) with labeled LPLC2 nuclei and transcripts of *dpr17* and *beat-VI* (**a**) and a single slice (0.5µm) from the light sheet projection (**b**, zoomed into the yellow dashed rectangular region); arrows indicate individual LPLC2 somas expressing markedly different levels of *dpr17* and *beat-VI*. D, dorsal; L, lateral.

c-d, Comparison of scRNA-seq (**c**) and HCR-FISH (**d**) measuring the correlation in expression for *dpr17* and *beat-VI* across LPLC2 neurons at 48h APF. Fitted lines represent the linear relationship between the two genes for each brain (FISH) or each wild type genotype (scRNA-seq); shaded regions represent 95% confidence intervals. r, Spearman's rank correlation coefficient.

d, expression patterns of selected genes (Fig. 2e) in LPLC2 from 24h to 96h APF. Plots show log-scaled normalized expression levels. Data from Kurmangaliyev et al., 2020.

e, Assessment of *dpr13* expression levels in individual sparsely labeled LPLC2 neurons using HCR-FISH. Right, cell bodies of dorsal, ventral, and central LPLC2 neurons, indicating the number of *dpr13* transcripts per cell. Inset, comparison of *dpr13* puncta counts in dorsal and ventral LPLC2 neurons. Dots represent individual neurons (1 neuron per brain). Error bars represent means ±95% confidence intervals.

f, Same as in (**e**), for *beat-VI*

g-h, Comparison of *dpr13* and beat-VI expression levels in dorsal and ventral LPLC2 neurons during UAS-*dpr13* (**g**) and UAS-*beat-VI* (**h**) overexpression in LPLC2. Dots, individual neurons (1-3 neurons per brain). Error bars represent means ±95% confidence intervals.

i-l, Assessment of Beat-VI and Dpr13 gradients at the protein level. Individual sparsely labeled LPLC2 neurons with dendrites sampling either dorsal, or ventral regions of the visual space, are co-localized with Dpr13(**i**) and Beat-VI (**k**) constitutive protein traps (GFP-fusion proteins). GFP levels in dorsal vs ventral cell bodies are measured via mean pixel intensity (**j, l**). Dots represent individual cells (N=5 for each location and condition). Error bars represent means ±95% confidence intervals.

Extended Data Figure 5 (related to Fig. 2)

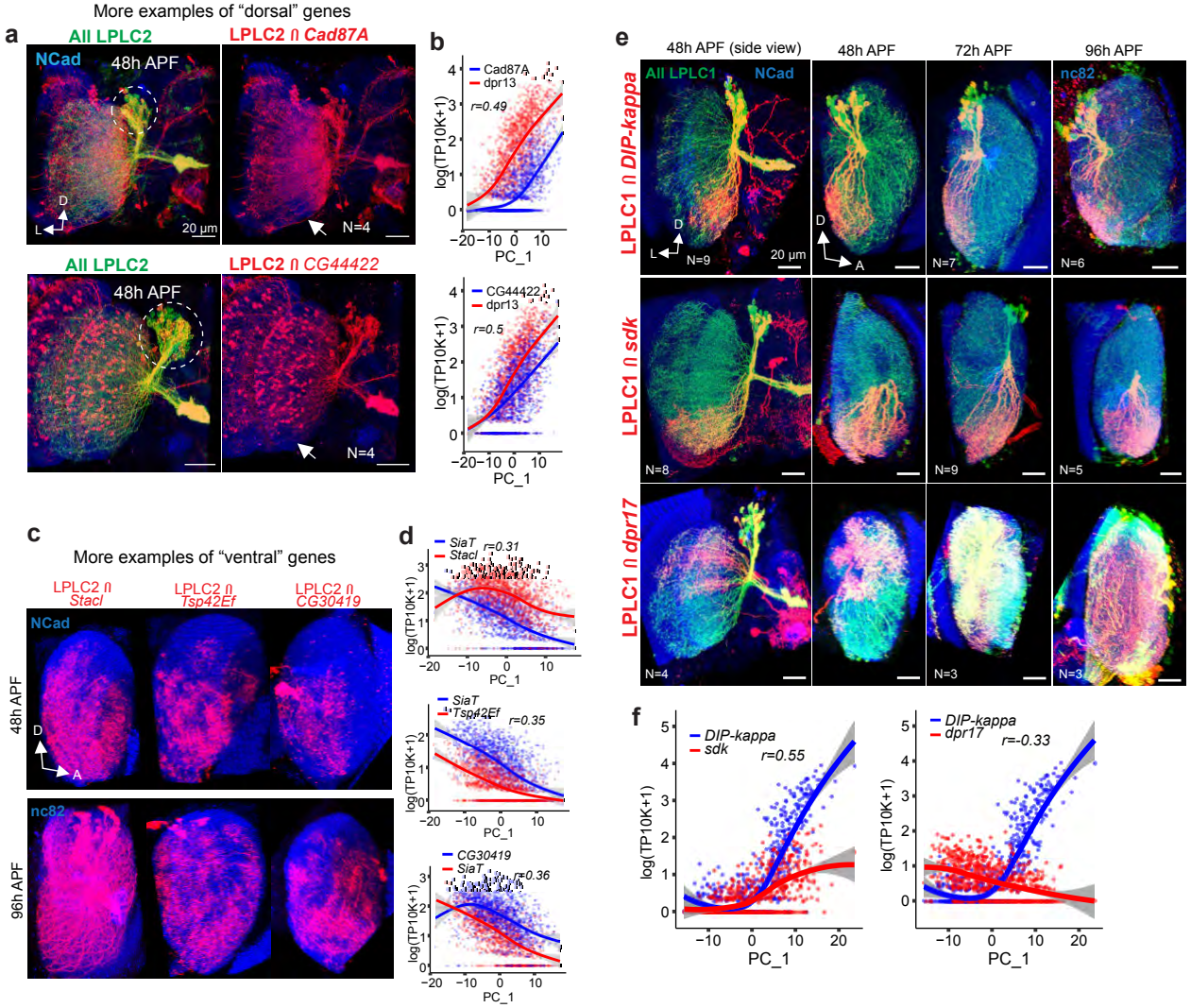

Extended Data Figure 5 (related to Fig. 2). Retinotopic correlates of molecular gradients in LPLC2 and LPLC1

a, Subsets of LPLC2 neurons expressing *CG44422* and *Cad87A* at 48h APF. White arrows indicate ventral regions of the lobula lacking expression of both *CG44422* and *Cad87A*. Dashed ovals, partial overlap of expression in somas, i.e., different LPLC2 neurons express different levels of *CG44422* and *Cad87A*. N, number of brains tested. D, dorsal; L, lateral.

b, Positive correlation between expression levels of *Cad87A*, *CG44422* and *dpr13* (inferred from scRNA-seq), along PC1 across the LPLC2 population at 48h APF, indicating that both *CG44422* and *Cad87A* can be considered “dorsal” genes.

c, Additional examples of genes expressed by ventral subpopulation of LPLC2 neurons. Red, dendrites of LPLC2 (lateral view of the lobula) that express stacl, *Tsp42Ef* and *CG30419* at 48h (top) and 96h (bottom) APF. D, dorsal; P, posterior.

d, Positive correlation between expression levels of *stacl*, *Tsp42Ef* and *CG30419* (inferred from scRNA-seq), along PC1 across the *LPLC2* population at 48h APF.

e, Retinotopically biased gene expression across LPLC1 neurons. Red, subsets of LPLC1 neurons expressing *DIP-kappa*, *sdk* and *dpr17* throughout development (posterior and lateral views of the lobula). N, number of brains tested. D, dorsal; M, medial; P, posterior.

f, Positive correlation between expression levels of *DIP-kappa* and *sdk* (top), and negative correlation between expression levels of *DIP-kappa* and *dpr17* (bottom), (inferred from scRNA-seq), along PC1 across the LPLC1 population at 48h APF, reflecting the retinotopically biased expression of these genes in (**e**).

Extended Data Figure 6 (related to Fig. 3)

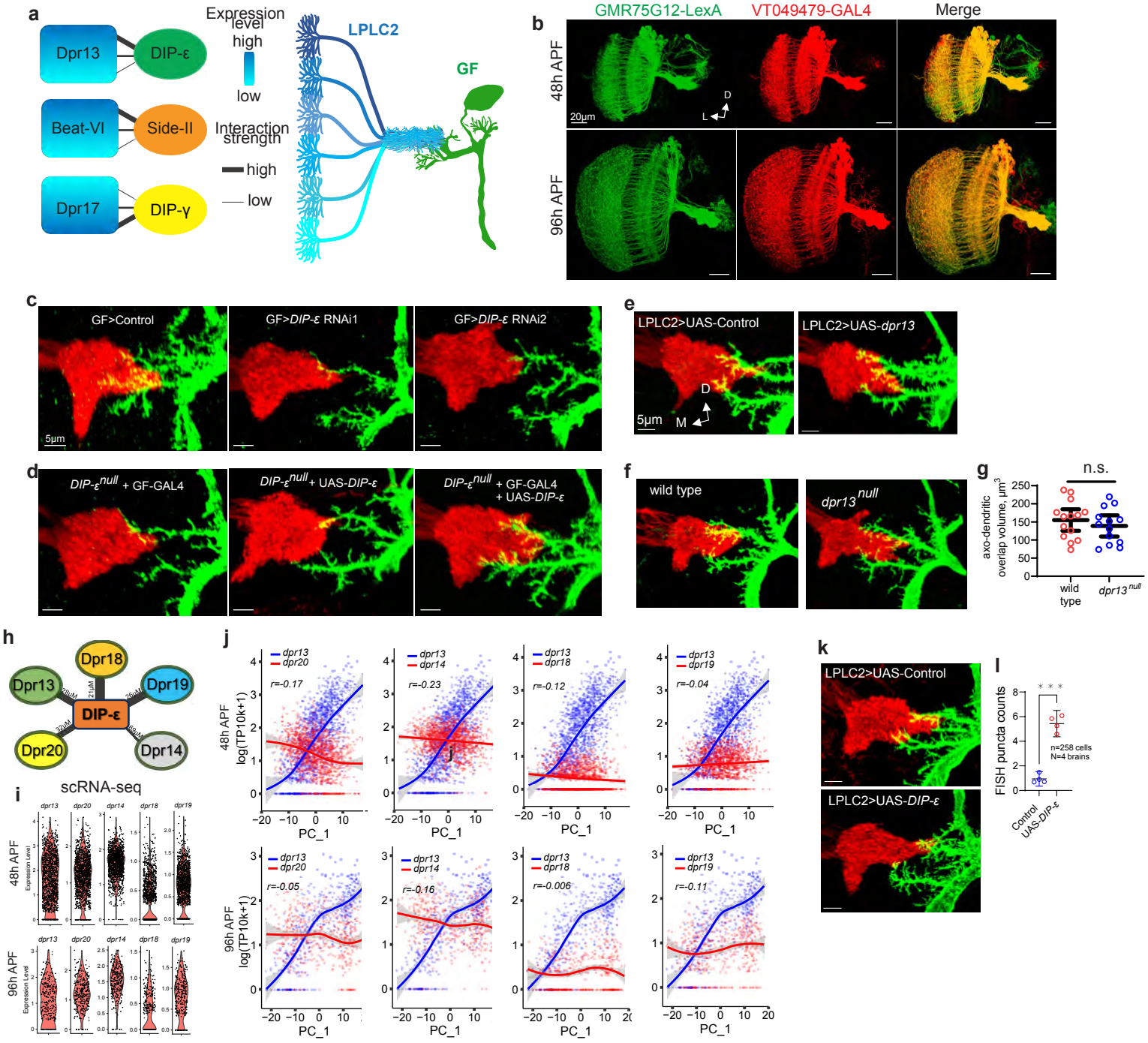

Extended Data Figure 6 (related to Fig. 3). Synaptic gradient between LPLC2 and the GF is established through a gradient of DIP-ε::Dpr13 molecular interactions.

a, Suggested model: to establish a synaptic gradient with LPLC2 based on dorsoventral expression gradient of any of the candidate molecules (Dpr13, Beat-VI, Dpr17), the GF needs to express a molecular binding partner to recognize one or more of these molecules.

b, Validation of VT049479-GAL4 expression in LPLC2 using GMR75G12-LexA as a reference. A complete overlap confirms that VT049479-GAL4 targets the entire LPLC2 population. D, dorsal; M, medial.

c, Confocal projections of LPLC2 axon terminals and the GF dendrites in wild-type animals, as well as animals expressing control RNAi and two different *DIP-ε* RNAi in the GF.

d, Same as (**c**). Rescue experiment: overexpression of DIP-ε cDNA in the GF in *DIP-ε*^{null} background (right) compared to two negative controls (left and middle).

e, Confocal projections of LPLC2 axon terminals and the GF dendrites in control animals and animals overexpressing *dpr13* in LPLC2

f-g, Confocal projections of LPLC2 axon terminals and the GF dendrites in wild type and *dpr13*^{null} animals **(f)** and comparison of axo-dendritic overlap volume between LPLC2 and the GF for these conditions **(g)**; Dots, individual brains. Error bars, means ±95% confidence intervals.

h, Protein interaction map showing binding strength (affinity values are inversely proportional to edge thickness) between DIP-ε and multiple Dprs expressed in LPLC2.

i, Expression levels of genes encoding DIP-ε binding Dprs in LPLC2 at 48h and 96h APF (inferred from scRNA-seq data generated in this study).

j, Correlation between expression levels of genes encoding DIP-ε binding Dprs in LPLC2 at 48h and 96h APF (inferred from scRNA-seq), along PC1 across the LPLC2 population at 48h and 96h APF.

k-l, Confocal projections of LPLC2 axon terminals and the GF dendrites in control animals and animals overexpressing *DIP-ε* in LPLC2 (**k**) and comparison of axo-dendritic overlap volume between LPLC2 and the GF for these conditions (**l**); dots, individual brains. Error bars, means ±95% confidence intervals.

Extended Data Figure 7 (related to Fig. 3)

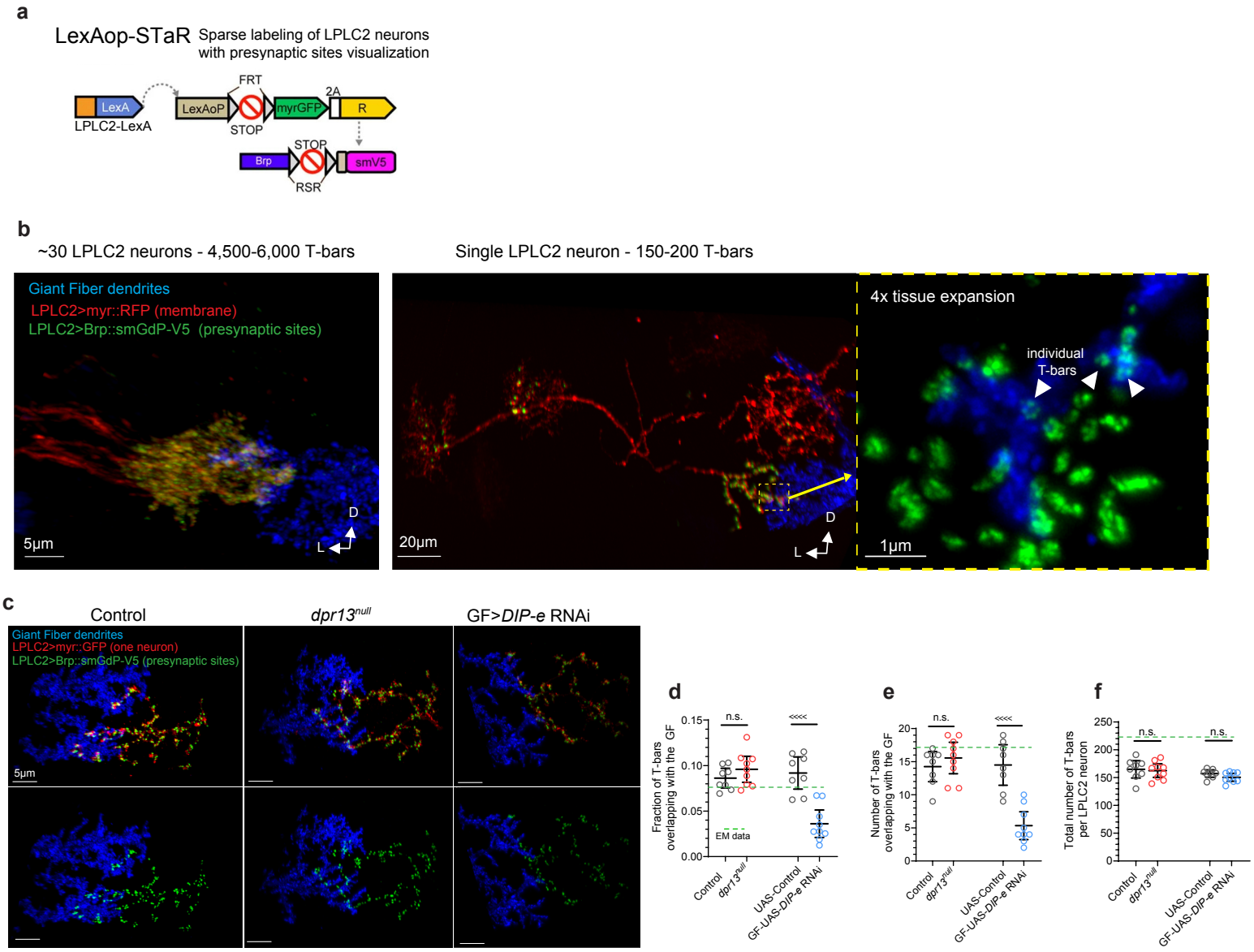

Extended Data Figure 7 (related to Fig. 3). Analysis of LPLC2-GF connections using synaptic labeling.

a, Genetic strategy (LexAop-STaR, **S**ynaptic **Ta**gging with **R**ecombination) for generating sparsely labeled clones of LPLC2 neurons (with a fluorescent membrane marker) and visualizing their presynaptic sites (T-bars) with Brp-smGdP-V5. Adapted from Dombrovski et al., 2023.

b, LPLC2 neurons labeled using LexAop-STaR. Left: confocal projection of LPLC2 glomerulus (axon terminals of ~30 LPLC2 neurons, labeled using long heat shock) co-localized with the GF dendrites. Middle: light sheet projection of a single LPLC2 neuron, imaged with 4x tissue expansion. Right: high-resolution image of the magnified view of presynaptic sites (T-bars) of a single LPLC2 neuron, co-localized with the GF dendrites. White arrows indicate individual T-bars, characterized by their distinctive ring-like shape and a typical diameter of 200–250 nm.

c, Light sheet projections of axon terminals from single LPLC2 neurons labeled with LexAop-STaR, imaged with 4x tissue expansion. Left to right: control animals, *dpr13*^{null} animals, and animals expressing DIP-ε RNAi in the GF.

d, Fraction of T-bars per single LPLC2 neuron overlapping with the GF dendrites. Left: control vs. *dpr13*^{null}; right: control vs. GF > UAS-*DIP-ε* RNAi. Dots represent individual neurons. Error bars indicate means ± 95% confidence intervals.

e, Same as in (**d**), measuring the number of T-bars overlapping with the GF dendrites.

f, Same as in (**d**), measuring the total number of T-bars per single LPLC2 neuron.

In **d–f**, green lines indicate corresponding values inferred from the hemibrain connectome reconstruction. In **d**, the discrepancy between connectome-based and anatomy-based values likely reflects additional T-bars in the lobula/lobula plate not included in this analysis.

Extended Data Figure 6 (related to Fig. 3)

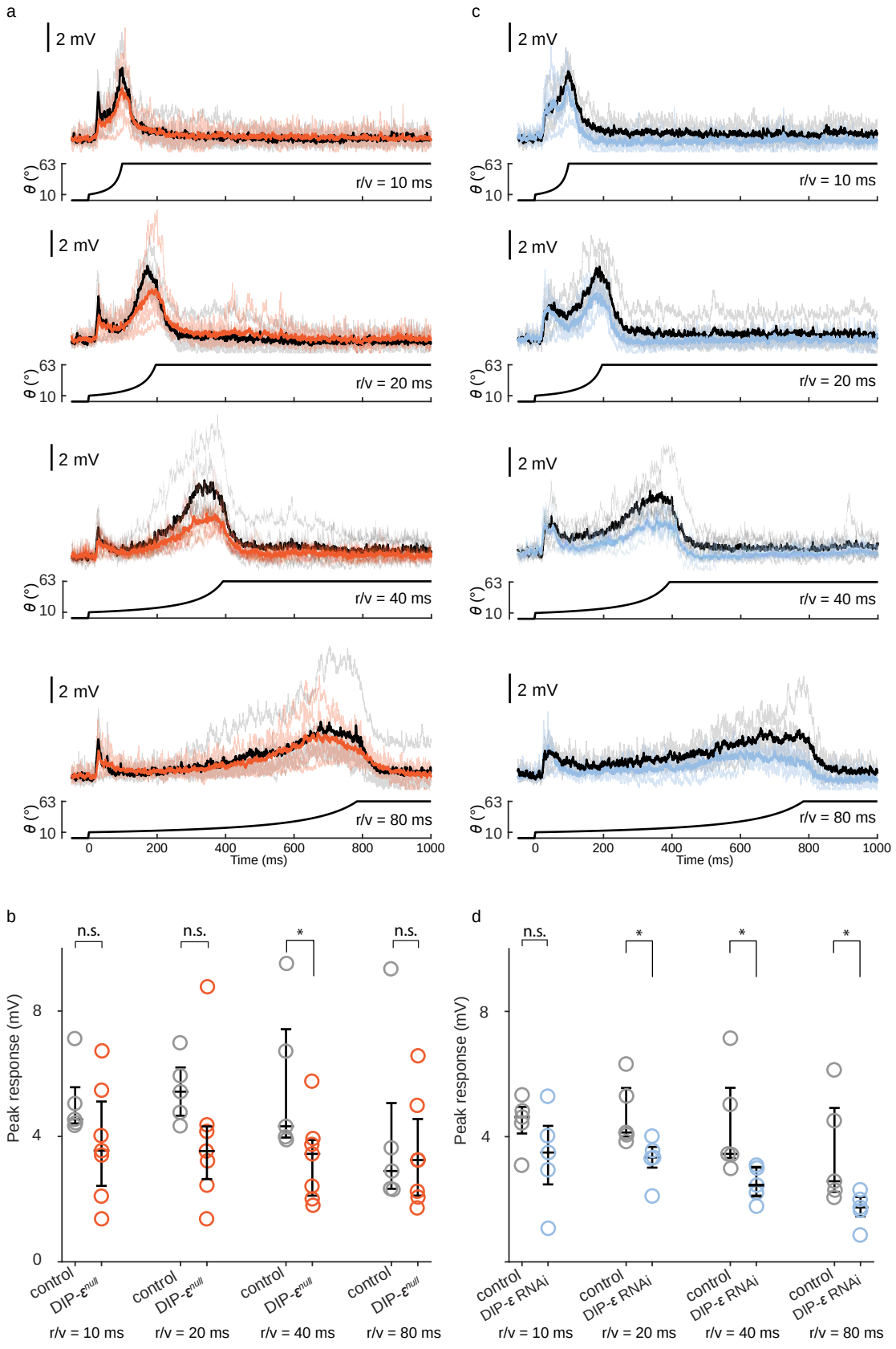

Extended Data Figure 8 (related to Fig. 3). Electrophysiology of the GF

a, GF responses to looming stimuli, in r/v = 10ms (top), r/v = 20ms (middle), r/v = 80ms (bottom). Control (average: black, individual fly: grey) and *DIP-ε*^{null} (average: orange, individual fly: light orange) traces are overlayed. Looming stimulus profile over time is displayed below the GF responses.

b, Quantification of expansion peak amplitudes in (**a**) from individual flies.

c, Same as (**a**) for controls (grey) and animals overexpressing *DIP-ε* RNAi in the GF (light blue).

d, Quantification of expansion peak amplitudes in (**c**) from individual flies.

Extended Data Figure 9 (related to Fig. 3)

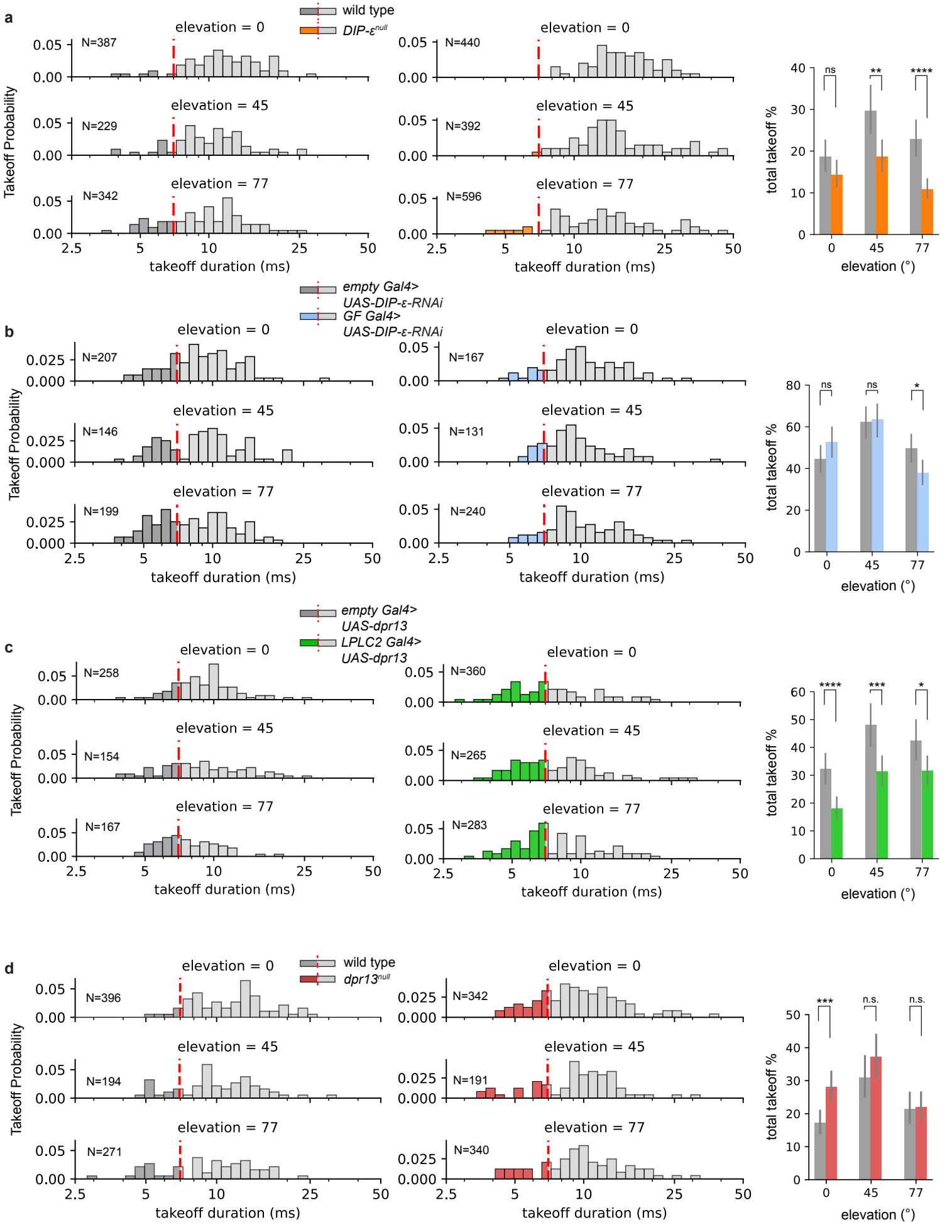

Extended Data Figure 9 (related to Fig. 3). Effects of Dpr13 and DIP-ε on GF-mediated takeoff behavior

a, Left, Histograms showing the distribution of takeoff sequence durations at different stimulus elevations (0°, 45°, and 77°) in wild-type (left, grey) and *DIP-ε*^{null} flies (right, orange). Short-mode and long-mode takeoffs are distinguished by red dashed lines. N, number of flies that performed a takeoff. Right, total takeoff percentages at different elevations for wild-type and *DIP-ε*^{null} flies. Error bars, 95% confidence intervals.

b, Same as (**a**) for controls (empty-Gal4 driving *DIP-ε* RNAi expression, left, grey) and flies expressing *DIP-ε* RNAi in the GF (right, blue).

c, Same as (**a**) for controls (empty-Gal4 driving expression of *dpr13*, left, grey) and flies overexpressing *dpr13* in LPLC2 neurons (right, green).

d, Same as (**a**) for controls (wild-type flies, left, grey) and *dpr13*^{null} flies (right, red).

Extended Data Figure 10 (related to Fig. 4)

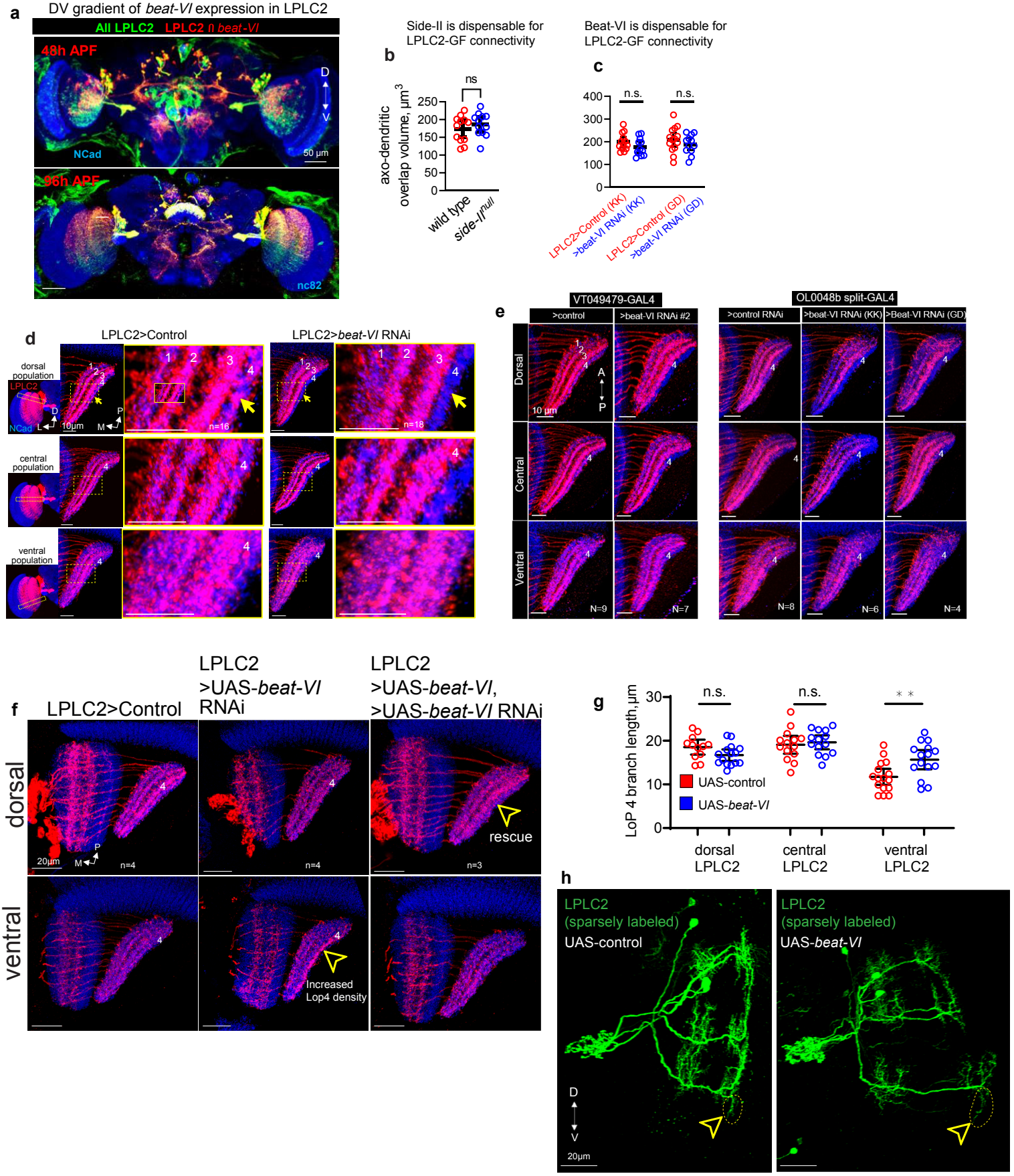

Extended Data Figure 10 (related to Fig. 4). Graded expression of *beat-VI* across LPLC2 neurons differentially affects LoP4 dendritic wiring.

a, Expression of *beat-VI* is biased towards the dorsal part of LPLC2 population. Red, subsets of LPLC2 neurons expressing *beat-VI* at 48h APF (top) and 96h APF (bottom). Green, all LPCL2 neurons. D, dorsal; V, ventral.

b-c, Comparison of axo-dendritic overlap volume between LPLC2 and the GF in *side-II*^{null} animals (**b**), and in animals with LPLC2 expressing beat-VI RNAi (**c**). Dots, individual brains. Error bars, means ±95% confidence intervals.

d, Confocal projections of LPLC2 dendrites (entire LPLC2 population labeled) in the lobula plate in control animals (left) and in animals with *beat-VI* RNAi expressed in LPLC2 (right). Leftmost panels, posterior views of the LPLC2 population with dashed rectangles indicating the location of cross-sections for dorsal, central, and ventral subsets of LPLC2. Numbers indicate LoP layers. Yellow arrows indicate LoP4 layer. D, dorsal; M, medial; L, lateral; P, posterior.

e, Same as (**d**) for two different LPLC2 GAL4 driver lines and two different *beat-VI* RNAi lines.

f, Confocal projections of LPLC2 dendrites (entire LPLC2 population labeled, dorsal and ventral cross-sections compared) in the lobula plate in control animals (left), animals overexpressing *beat-VI* cDNA (middle), and animals overexpressing *beat-VI* cDNA while also expressing *beat-VI* RNAi (right). Yellow arrowheads indicate changes in LoP4 dendritic density.

g, Length of LoP4 dendritic branches for dorsal, central and ventral LPLC2 neurons in control and LPLC2>UAS-*beat-VI* flies. Dots, individual neurons. Error bars, means ±95% confidence intervals.

h, Confocal projections of sparsely labeled LPLC2 neurons. Representative images of control animals (left) and animals overexpressing *beat-VI* in LPLC2 (right). Differences in the length of LoP4 dendritic branches across ventral LPLC2 neurons are highlighted.

Extended Data Figure 11 (related to Fig. 4)

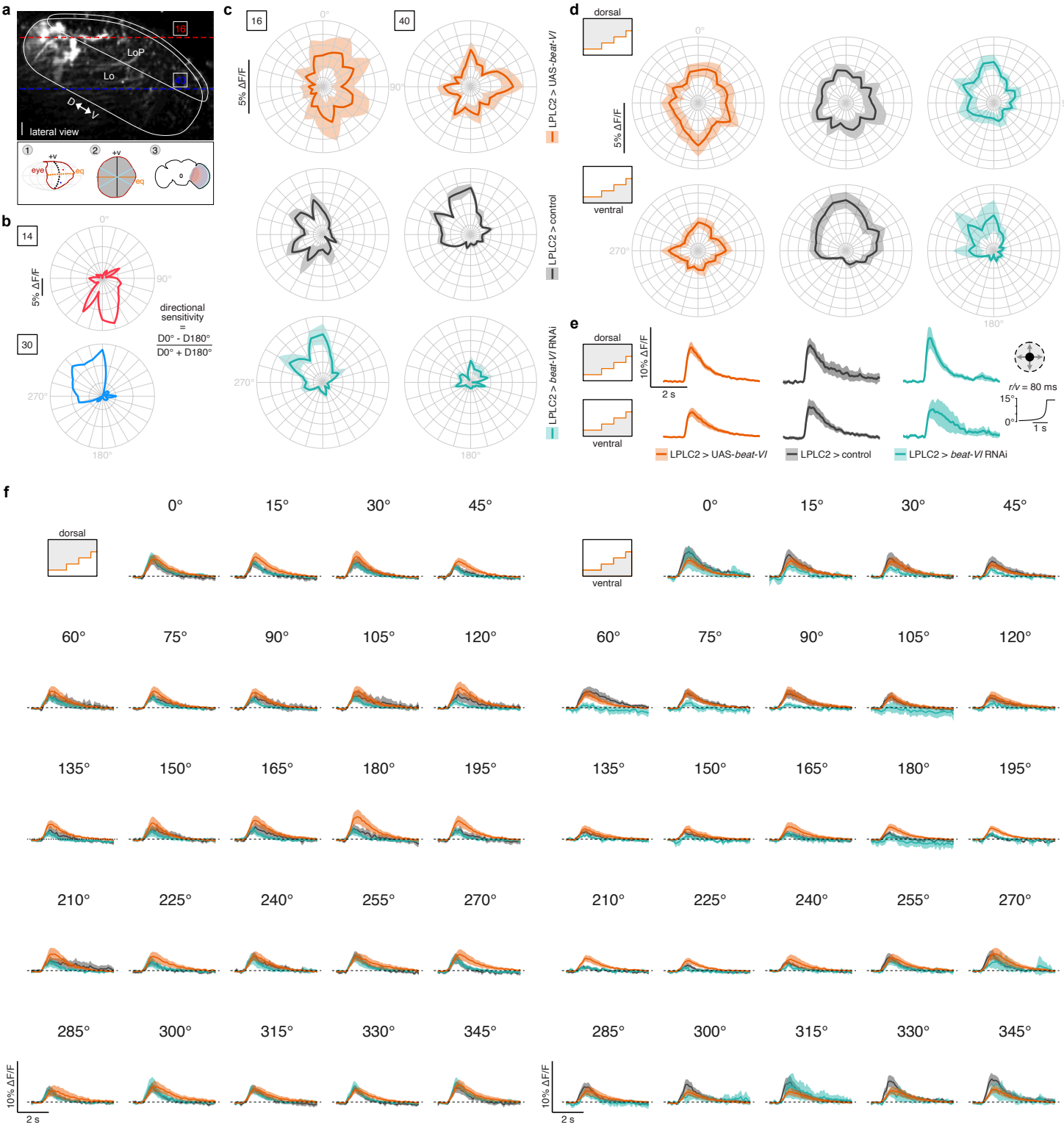

Extended Data Figure 11 (related to Fig. 4). Beat-VI::Side-II molecular gradient regulates T4d/T5d-LPLC2 synaptic gradient.

a, 3D reconstruction of LPLC2 neurons from a Z-stack taken using the two-photon microscope in a head-fixed fly (lateral view, scale bar: 10 μm). Dashed lines highlight the two Z-planes where LPLC2 dendrites responded to dark looming at positions 16 (red) and 40 (blue) on the LED display (top). White solid lines approximately define the reference neuropils. Schematic of the procedure used to identify the putative neurons in the fly connectome stimulated by two representative grid positions (bottom, see Methods).

b, Polar plots of the peak responses to moving dark edges in dorsal (14) and ventral (30) regions in two representative flies (color-coded by position).

c, Polar plots of the average peak responses to moving dark edges in dorsal (16) and ventral (40) regions for control, LPLC2>*beat-VI* RNAi, and LPLC2>UAS-*beat-VI* flies. Error band, s.e.m.

d, Polar plots of the average peak responses to moving dark edges in aggregated dorsal (above the equator) and ventral (below the equator) regions for control, LPLC2>*beat-VI* RNAi, and LPLC2>UAS-*beat-VI* flies. Error band, s.e.m.

e, Average calcium transient in response to a dark looming in dorsal (above the equator) and ventral (below the equator) regions for control, LPLC2>*beat-VI* RNAi, and LPLC2>UAS-*beat-VI* flies. Error band, s.e.m.

f, Average calcium transients in response to dark edges moving in 24 (from 0° to 345°) different orientations for control, LPLC2>*beat-VI* RNAi, and LPLC2>UAS-*beat-VI* flies. Dorsal (left) and ventral (right) regions. Error band, s.e.m.